Abstract

The Light at the End of the Tunnel Junction - Improving the Energy Resolution of UV Single-Photon Spectrometers using Diffusion Engineering

Veronica Andreea Savu

Yale University

2007

We present experimental results which test whether diffusion engineering can increase the energy resolution of a single-photon superconducting tunnel-junction spectrometer. When a UV photon is absorbed in superconducting Al, it creates an excess number of quasiparticles. If the superconducting absorber is the electrode of a tunnel junction, the quasiparticles tunnel across the voltage-biased junction. The collected charge is proportional to the number of excess quasiparticles. For small energy photons, the initially-created charge can be amplified by backtunnelling. The quasiparticles confined around the junction can backtunnel as holes after tunnelling, doubling the output charge, and then tunnel again. The charge multiplication is proportional to the confinement time. When the counterelectrode is terminated with a long, narrow lead, the quasiparticles diffuse out on a time scale set by the dimensions of the leads and of the electrodes, and the diffusion constant of the material. We show how the charge created by the photon varies with the purity of the Al film and with different lead geometries. The experimental results are compared to theoretical predictions of our model. We achieve an energy resolving power of 3 for a photon energy of 3.68 eV. Further investigation of losses in our materials should improve the energy resolution of our diffusion-engineered devices.

The Light at the End of the Tunnel Junction - Improving the Energy Resolution of UV Single-Photon Spectrometers using Diffusion Engineering

A Dissertation

Presented to the Faculty of the Graduate School

of

Yale University

in Candidacy for the Degree of

Doctor of Philosophy

by

Veronica Andreea Savu

Dissertation Director: Professor Daniel E. Prober

May 2007

Table of Contents

List of Figures

List of Tables

List of Symbols

Δ	superconducting energy gap
ΔE	total energy resolution (measured at FWHM)
ΔE_{elec}	energy resolution due to electronic noise extrinsic to the device
$\Delta E_{electrical}$	energy resolution due to electrical noise
ΔE_{flux}	energy resolution due to photons absorbed outside the absober
ΔE_{Fano}	energy resolution due to F
ΔE_{tunn}	energy resolution due to G
ε	mean energy to produce a quasiparticle
Γ	rate constant
Ω	phonon energy
Ω_D	Debye phonon energy
σ	conductivity
τ	time constant
τ_{out}	outdiffusion time
τ_{tunn}	tunnelling time

A_j	junction area
c	constant of proportionality
C	capacitance
d	Al thickness

d_{ox}	thickness of the junction oxide
d_{r1}	thickness of the first resist layer
D	diffusion constant
D_{qp}	quasiparticle diffusion constant
e	electron's charge
e	base of natural logarithm
eV	electron volt
E_{photon}	photon energy
f(E)	Fermi distribution function
E	quasiparticle energy
E_k	energy of quasiparticle with momentum $\hbar k$
F	Fano factor
G	factor representing the variation in the number of tunnellings for a quasiparticle
$\hbar$	Planck's constant divided by 2π
^{3}He	isotope of helium with atomic mass of 3
^{4}He	isotope of helium with atomic mass of 4
i_n	current noise
I_{dc}	dc STJ quiescent current
I_C	critical current of the junction
j_C	junction critical current density
k	wave vector
k_B	Boltzmann's constant
k_F	Fermi wave vector
l	outdiffusion lead length
L	electrode length
m	electron mass
M	tunneling matrix element

n	quasiparticle density
N	quasiparticle number
p	charge multiplication factor
Q_i	initial charge created by photon
Q_0	offset charge
R_n	resistance of STJ in normal state
R	recombination constant
T	temperature
T_C	critical temperature
w	outdiffusion lead width
W	electrode width
V_b	bias voltage
Vol	volume

Acknowledgements

This dissertation was only possible with the help of many people. I would first like to thank my advisor, Daniel E. Prober, for his support throughout my years of graduate school. His teaching, experimental skills and intuition as a physicist provide a model I hope some day to achieve. Luigi Frunzio has also provided extraordinary help and counsel since the beginning of this project.

The other members of the Prober lab have contributed invaluably to my research. Chris Wilson immersed me in the subtleties of the experiment, and set an excellent example for me to follow. I am also indebted to Liqun Li for having patiently taught me the physics of the project. I benefited from many technical discussions with Matt Reese and enjoyed our countless hours together. Bertrand Reulet, the excellent physicist with whom I shared lab space, brought warmth and wisdom. Daniel Santavicca and Anthony Annunziata were fantastic colleagues who contributed to a stimulating intellectual atmosphere in Becton 405. Aviad Frydman and Misha Reznikov were great friends and mentors during their year as members of the group. Stephan Friedrich and Ken Segall offered their insights and experience at important moments during the project. Thanks also to the junior member of our group, Joel Chudow, and to the two undergraduate students who assisted me during summer research, Ivan Borzenets and Jonah Waissman.

I thank my dissertation committee members, Karyn Le Hur, Simon Mochrie, Robert Schoelkopf, and Andrew Szymkowiak for their careful reading and insightful comments, which have greatly strengthened the final version of the thesis. Caroline Kilbourne at Goddard Space Flight Center, who served as the outside reader, gave me excellent feedback on

a very tight schedule.

Many other members of the Yale faculty have contributed to my rich experience as a graduate student. I received much useful advice regarding optics from Bob Grober. I learned a lot from Kurt Gibble during the year I spent in his lab before he moved on to a tenured position at Penn State. I learned how to be a better teacher from my interactions with Michel Devoret, Peter Kindlmann, Ramamurti Shankar, Meg Urry, and Alex Zeller. My professors at Caltech and Irina Calomfirescu, my Physics teacher at Mihai Viteazul high-school in Bucharest, also contributed to my growth as a scientist.

The fourth floor of Becton was enlivened by many graduate students and postdocs, from whom I have received help in innumerable ways, small and large: Aric Sanders, Minghao Shen, Julie Love, John Teufel, Ben Turek, Vijay (a.k.a. Rajamani Vijayaraghavan), Irfan Siddiqi, Mike Metcalfe, Hannes Majer, Andreas Walraff, Etienne Boaknin, David Schuster, Lafe Spietz, Chad Rigetti, and Vladimir Manucharyan. I owe special gratitude to the administrative staff for years of help and warm friendship: Maria Gubitosi, Theresa Evangeliste, Jo-Ann Bonnett, and Jayne Miller.

I particularly enjoyed the friendship and support of the small group of exceptional women with whom I started my studies in the Yale Physics Department in September 2000: Betty Bezverkhny Abelev, Sarah Bickman, Grace Chern, and Sevil Salur. Betty and Veronica became so close that we have been immortalized in the popular culture with our own comic strip and t-shirts. Sam Bench, one of the few other women on the fourth floor of Becton, has been a friend since undergraduate days at Caltech. I am grateful for the friendship of Stefania Marin, which added joy to my life in New Haven. The Romanian community in New Haven has also been a constant source of support and comradery.

My mother and father, Maria Andreea and Nicusor Savu, gave all of themselves to raising me. Though it has meant great distance from their only child for a decade, they encouraged and supported me to pursue an independent career in the United States. My husband, Martin Benjamin, who I met and married during my time at Yale, offered me a

tremendous amount of moral support and love. He put his linguistic experience to good use by proofreading the first version of my dissertation. I dedicate this thesis to him and to my parents.

Chapter 1

Introduction

1.1 Overview

Superconducting tunnel junctions (STJs) have been used for over a decade as single photon spectrometers. The gap energy in superconductors is on the order of 1 meV, three orders of magnitude smaller than in semiconductors. Thus, for the same energy photon absorbed, there are many more excitations created in a superconductor than in a semiconductor. This offers the potential for better energy resolution using superconductors instead of the conventional semiconductors. A further advantage of superconductors is that their typical Debye energies (tens of meV), which are a measure of the maximum phonon energy, are much larger than their energy gaps. Thus, the phonons generated by an absorbed photon participate in the creation of excess excitations. These advantages led to a sustained effort in the photon detector community. The detectors were initially developed for X-ray photons. Most of the experiments used the Mn K_α and K_β lines of a ^{55}Fe source, with an energy of 5.89 keV and 6.49 keV. In 1986 Twerenbold and colleagues achieved an energy resolution of 65 eV at 6 keV with Sn tunnel junctions [Twerenbold1986]. As the energy resolution for X-rays improved, the STJ-based detectors have been developed for lower-energy photons, all the way from soft X-rays down into the near infrared (NIR) range.

Astronomy has already benefitted from the use of STJ-based single photon spectrome-

ters [Bruijne2002]. The photon's energy (color) as well as its arrival time can be recorded, at a relatively high counting rate. Thus, transient weak signals from distant sources can be explored, such as visible light from pulsars and variable stars. The change in brightness of several spectral channels can be recorded in parallel, on millisecond to microsecond timescales [Rando2000].

In biology, measurement of fluorescent spectra at the single-photon level is a challenging issue [Nagl2005]. For imaging low intensity fluorescent specimens, avalanche photodiodes (APDs) are usually used. For obtaining spectral information, an APD has to be used with a set of narrow-band filters. Every time the band filter is changed, one can record data at a specific wavelength. For studying multiple chromophores, the sample has to be scanned multiple times, increasing its probability of photobleaching. On the other hand, dispersive gratings have as many as 32 energy channels [LSM510], but they are read sequentially with only one photomultiplier tube (PMT). Simultaneous read-out of all the channels would require a high level of experimental complexity.

The development of ultra-sensitive, fast spectrometers for single UV and optical photons would benefit many applications from a wide range of research fields. In addition to this practical goal, improving the modelling of the physical processes inside the STJ-based detectors should deepen our understanding of the basic physics of non-equilibrium quasiparticle processes in superconductors.

1.2 Operating Principle of the Detector

Our detectors have two main functional parts: a superconducting absorber and a superconducting tunnel junction. For the work presented in this thesis, the role of the absorber is played by the Al electrodes of an Al/Al-oxide/Al junction. In a Josephson junction there is a maximum Cooper pair tunneling current, called the supercurrent or the critical current I_C. For larger currents a voltage develops across the junction. Figure 1.1 shows

the current vs. voltage characteristic of a Josephson tunnel junction with the Cooper pair current. In our experiments, the Cooper pair tunnel current must be suppressed in order to enable stable voltage biasing of the junction [Friedrich97IEEE]. We suppress the pair tunnel current by applying a magnetic field parallel to the plane of the junction. We apply a bias voltage and monitor the current due to the thermally excited quasiparticles tunneling across the junction. This quiescent current decreases exponentially with the inverse of the temperature. Figure 1.2 shows the simulated thermal current in a device for two different bath temperatures, after the critical current has been totally suppressed, a zoom-in around the origin of Figure 1.1 without the critical current branch.

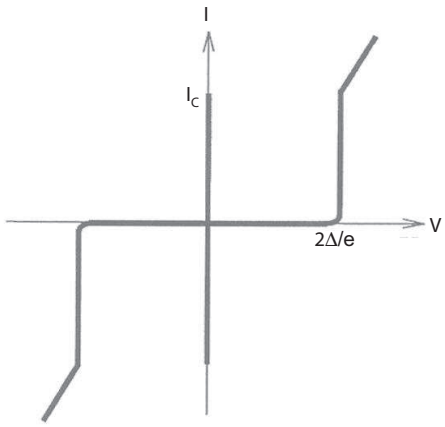

Figure 1.1: Simulated current vs. voltage characteristic (using the BCS theory) of an STJ with unsuppressed Cooper pair current.

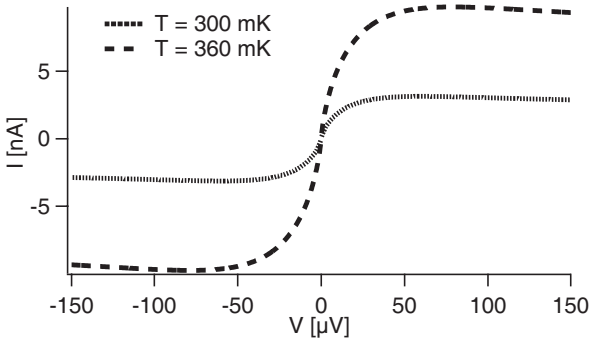

Figure 1.2: Current vs. voltage characteristic of an STJ with suppressed Cooper pair current.

An absorbed photon with energy E_{photon} larger than twice the gap energy Δ breaks Cooper pairs and creates an excess number of quasiparticles N, proportional to its energy. These excess quasiparticles tunnel across the barrier, being recorded as a current pulse in addition to the dc (thermal) tunneling current, as shown in Figure 1.3b. By integrating the pulse, we obtain a charge from which we infer the energy of the absorbed photon. The maximum count rate is the inverse of the reset time of our spectrometer. Once the excess quasiparticle pulse has completely decayed, the detector is ready to respond to the next absorbed photon.

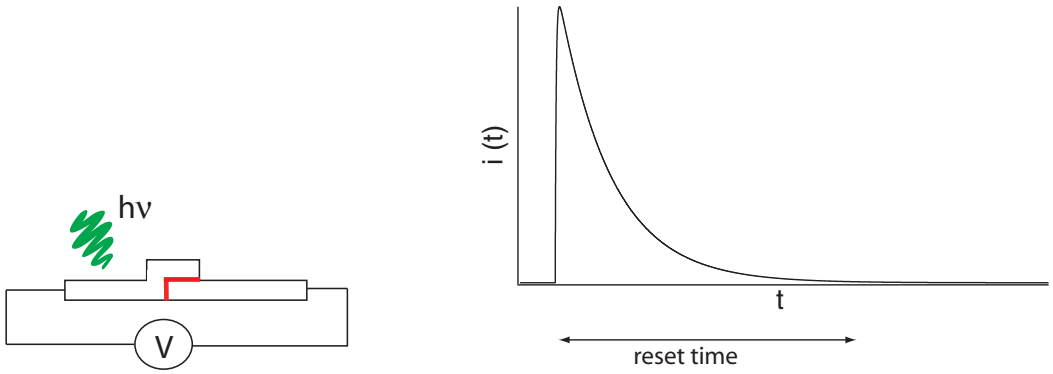

(a) Detector schematic, showing a voltage-biased junction under impinging photon.

(b) Pulse created by absorbed photon.

Figure 1.3: An absorbed photon in one electrode of an STJ creates excess quasiparticles that tunnel across the voltage-biased junction, recorded as a current pulse.

For small-energy photons the induced current is small, and therefore our detector has to be more sensitive. Our detector noise has two components: electrical readout noise and intrinsic device noise. Both degrade the sensitivity with which we can resolve an initially created charge, by increasing the charge noise. The electrical readout noise depends on the electrical bias and read-out circuit. The intrinsic device noise includes the shot-noise of the quiescent current, $\sqrt{2eI_{dc}}$, and the statistical noise of the photon-induced current.

The statistical noise of the induced signal imposes a fundamental limit on the energy resolution in tunnel junctions. Due to the probabilistic nature of the quasiparticle produc-

tion, an absorbed photon with the same energy E_{photon} will create a different number of quasiparticles N for every absorption event. This fluctuation around the average number of created quasiparticles $< N >$ is detrimental to the energy resolution of the STJ. This is quantitatively expressed in the form of the Fano factor F= $\frac{(N- < N >)^2}{< N >}$. F was calculated to be 0.2 for Sn [Kurakado1982] and Nb [Rando1992] and should have a similar value for all bulk superconductors. The Fano factor sets a minimum energy resolution:

$$\Delta E_{Fano} = 2.355\sqrt{F\varepsilon E_{photon}} \tag{1.1}$$

where ε is the average energy necessary to create a quasiparticle [Kurakado1982]. The factor of 2.355 converts the one standard deviation to full width at half maximum (FWHM). For Al and other low-gap superconductors, ε is calculated to be 1.7Δ [Kozorezov2000].

Quasiparticles can tunnel multiple times before they are lost to recombination or other processes. The probability for tunnelling out of the electrode i, for $i = 1,2$ is P_i. P_i can be expressed in terms of the quasiparticle rates as:

$$P_i = \frac{\Gamma_{tun\,i}}{\Gamma_{tun\,i} + \Gamma_{rec\,i} + \Gamma_{loss\,i}} \tag{1.2}$$

where $\Gamma_{tunn\,i}$ is the tunnelling rate, $\Gamma_{rec\,i}$ is the effective quasiparticle recombination rate, and $\Gamma_{loss\,i}$ is a temperature-independent quasiparticle loss rate due, for example, to outdiffusion or to loss in volumes of trapped flux. The probability for a single tunnelling event is $P(1) = P_1(1-P_2)$. The probability for a quasiparticle to tunnel, backtunnel and then be lost is $P(2) = P_1P_2(1-P_1)$. Hence the average number of times the quasiparticles tunnel, $\overline{n}$, is:

$$\overline{n} = \sum_{n=0}^{\infty} nP(n) = \frac{P_1(1+P_2)}{(1-P_1P_2)} \tag{1.3}$$

The variation in the average number of times a quasiparticle tunnels was calculated [Goldie1994] and is expressed by a factor G which adds to the minimum attainable energy resolution:

$$\Delta E_{tunn} = 2.355\sqrt{G\varepsilon E_{photon}} \tag{1.4}$$

For our devices, G is computed to be of order unity.

The total energy resolution due to the quasiparticle statistical processes adds in quadrature with the energy resolution imposed by other electrical noise sources $\Delta E_{electrical}$:

$$\Delta E_{tot} = \sqrt{\Delta E_{Fano}^2 + \Delta E_{tunn}^2 + \Delta E_{electrical}^2} \tag{1.5}$$

Both F and G represent statistical noise sources which set a limit on detecting low-energy photons with good energy resolving power ($E_{photon}/\Delta E$). However, in an STJ there is a remarkable process which allows intrinsic charge multiplication, effectively increasing the signal created by a photon. A quasiparticle is a linear superposition of an electron and a hole. As shown in Figure 1.4, it can tunnel as an electron from electrode 1 to electrode 2, and it can backtunnel as a hole from electrode 2 to electrode 1, in both cases gaining energy eV_b from the bias voltage V_b. This one quasiparticle transfers two negative charges from left to right, such that the measured number of electrons exceeds the initial excess quasiparticle number Q_i/e. This is the 'Gray effect' [Gray1978], also known as backtunnelling. The same quasiparticle can continue tunnelling and backtunnelling, increasing the detected charge, pQ_i, until it either recombines or diffuses away from the junction area. The charge multiplication factor p is the ratio of the residence time of the quasiparticles in the electrodes to the tunnelling time.

Previous research in our group studied devices with a large multiplication factor, $p \approx 50$. This was achieved by confining the quasiparticles with higher-gap materials on each side of the electrodes. This 'gap-engineering' approach introduced Joule heating in our junctions. In a single-tunnelling junction, once the quasiparticles tunnel, they quickly diffuse away from the junction into wide leads. In the gap-engineered devices, the quasiparticles keep tunnelling and backtunnelling, until they are lost through recombination. Upon tunnelling they gain energy from the bias voltage. They scatter inelastically by emitting phonons, thus relaxing down in energy. The scattering time decreases with the cube of the initial energy, such that quasiparticles of energy 4Δ take several nanoseconds

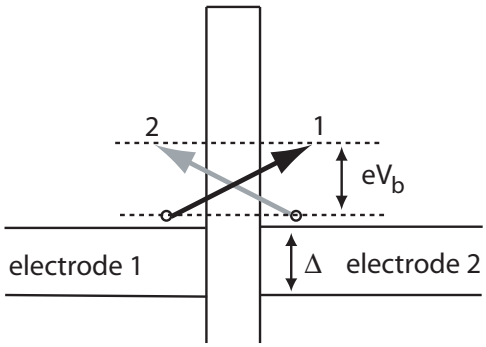

Figure 1.4: Energy band diagram of a junction in a modified excitation representation. The arrows illustrate quasiparticle tunnelling events. The quasiparticles tunnel as electrons from left to right, gaining the bias energy $\mid eV_b \mid$, as showed by the darker arrow in process 1. They backtunnel as holes from right to left, gaining the bias energy $\mid eV_b \mid$, as showed by the grey arrow in process 2.

to emit a phonon [Segall2004]. Not all of them relax down to the energy gap level before they backtunnel. After multiple tunnellings, some of the quasiparticles have energies larger than 3Δ. These can generate excess quasiparticles by emission of 2Δ or larger phonons. These phonons break pairs and cause an increase in the dc current, like heating. This effect was seen in our gap-engineered devices, increasing the shot current noise in our measurement.

In the case of STJ-based spectrometers which use larger-gap leads on each side of the junction to promote backtunnelling, there is an additional noise source which limits the energy resolution [Wilson2001]. This is the thermal generation-recombination noise, due to the thermodynamic fluctuations of the quiescent quasiparticle number in the electrodes.

Implementing a moderate charge multiplication factor could reach an optimum signal-to-noise ratio. The signal would increase according to the charge multiplication factor, without too much heating. The present research tested this hypothesis by using diffusion-engineered devices. The quasiparticles are confined in the left electrode by the higher-gap material, tantalum (Ta), which acts like a plug, in the same way as in the gap-engineered devices, as seen in Figure 1.5. The right electrode is continued with a long, narrow lead, made from the same material as the electrodes. We expect the energy resolution of this

device type to be limited only by the statistical noise sources. The quasiparticle residence time here is dictated by the time it takes them to diffuse out the narrow lead, called the out-diffusion time. The out-diffusion time is a function of the material diffusion constant, the lead dimensions, and its relative size compared to the electrode size. By changing the wire geometry, we can control the out-diffusion time. This allows us to test regimes with different charge multiplication factors by implementing different lead designs.

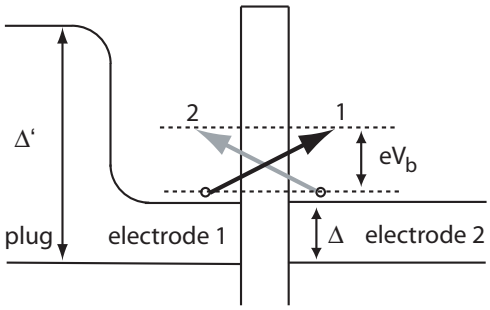

Figure 1.5: Energy band diagram of a junction with a higher-gap material plug on the left side, in the modified excitation representation.

1.3 Previous Group Research and Concurrent Work

Michael Gaidis [Gaidis1994] started the work on STJ detectors at Yale. He developed the initial design, fabrication process, electrical characterization and testing of high quality STJ detectors for X-ray photons. Using a charge pulse amplifier, he obtained an energy resolution of 190 eV for 6 keV X-rays.

Stephan Friedrich [Friedrich1997] tested double-junction devices for X-rays, achieving spatial resolution for the absorbed photon in the absorber. He constructed a lower-noise, more stable electronic circuit. When combined with the imaging detectors, the energy resolution reached 54 eV at 6 keV. The new current pulse amplifier allowed for extraction of relevant quasiparticle time scales.

Kenneth Segall [Segall2000] further improved the electronics and experimental setup, while developing a detailed microscopic model for the detectors. An energy resolution of

26 eV at 6 keV was achieved. Quantifying all the device noise sources and developing the microscopic model were an important step towards developing a better detector.

Liqun Li [Li2002] continued testing of X-ray imaging devices, using improved designs and lowering the electronic noise even more. From device physics studies, the diffusion constant and quaisparticle lifetime in the Ta absorber were extracted. It was her work that triggered the idea of implementing controlled outdiffusion for increasing backtunnelling in our devices: X-ray data showed a slower than expected pulse decay time for a device connected through a narrow lead to the wiring pads. The best energy resolution was 13 eV at 6 keV.

Christopher Wilson [Wilson2002] tested both imaging and single-junction optical detectors. He developed a detailed model that relates the thermodynamic fluctuations in the junction electrodes to the device excess current noise. From thorough modelling and analysis of the backtunnelling device data, his conclusion was that having less backtunnelling could alleviate the self-heating effect present in the strong backtunnelling devices. The strong backtunnelling, double-junction detector exhibited a very good energy resolution of 1.5 eV at 4.89 eV over the whole $10 \times 100\ \mu m^2$ Ta absorber, when tested with photons from a Hg lamp. For the non-backtunnelling devices tested with laser pulses, the electronic noise $\Delta E_{electrical}$ was 2.14 eV. The total noise ΔE was fit by adding the electronic noise in quadrature with ΔE_{flux} extra noise due to the photon flux, $\Delta E = \sqrt{(\Delta E_{elec}^2 + \bar{N}\Delta E_{flux}^2)}$. The extra noise ΔE_{flux} was found to be 1.3 eV per absorbed photon. The laser photons had an energy of 3.68 eV.

The European Space Agency (ESA) developed a 12×10 pixel array of STJs, called S-Cam 3, for ground-based astronomy, deployed at the 4.2 m William Herschel telescope in La Palma, Spain. The devices use a stack geometry with Ta/Al electrodes. The photon is absorbed in the Ta layer. The excess created quasiparticles diffuse into the Al electrode, where they are trapped by energy relaxation. They tunnel and backtunnelling multiple times across the Al/Al-oxide/Al junction, increasing the collected charge. They are con-

fined around the junction area because of the higher-gap Ta 'plugs'. The measured resolving power averaged over all the channels was 10 at 2.48 eV [Verhoeve2006] for a pulse time of 20 μs.

1.4 Thesis Organization

In this thesis we present the work done on developing high energy resolution single UV photon detectors based on Al/Al-oxide/Al STJs using diffusion engineering.

Chapter 2 introduces the basic device physics. The concept of diffusion engineering is explained. We start with a simple, intuitive analytical model and describe its electrical equivalent. A more complex simulation of the diffusion process is presented and we compare it to the simpler model. Using a diffusion engineering flowchart, we comment on the requirements necessary for maximizing our device signal-to-noise ratio, which leads to competing trends for certain parameters. We show how we optimized the values for these parameters.

Chapter 3 describes the experimental setup, including cryogenics, electronics, electromagnetic shielding, optics and data acquisition procedures.

Chapter 4 explains in detail the fabrication techniques and parameters used for making the devices tested in this thesis. The main 3-layer processing is presented in an easy to understand, non-chronological order: first the resist processes for each layer, followed by the metal deposition steps for each layer. The device layout is explained and optical and electron-beam pictures of relevant devices are included.

Chapter 5 presents the research path followed in this work. The present research started with the development of a new STJ fabrication technique, necessary for reaching the requirements for this project. The different device generations and the reasoning behind the changes in their design and fabrication are reviewed. Results from the most relevant devices are presented and analyzed.

In Chapter 6 we discuss the performance of our devices and the main obstacles en-

countered. We suggest alternative approaches for future work on detector development.

The Appendices provide additional information regarding experimental film properties, device parameters, and a summary of the experimental results.

Chapter 2

Theory

2.1 Intrinsic Quasiparticle Non-equilibrium Processes

2.1.1 Quasiparticle Generation

Radiation detectors consist of an absorber and a readout. The energy deposited in the absorber is converted into excitations. These are registered by the readout which outputs a signal proportional to the amount of deposited energy. In the energy range for which the detector is designed, the absorber must be efficient in absorbing radiation and transferring the resulting excitations to the readout. In our STJ spectrometer, the main absorbers are the superconducting Al electrodes and the readout is the superconducting tunnel junction. The impinging photon deposits its energy in the absorber, where it is converted into excess phonons and quasiparticles. The excess quasiparticles tunnel across the voltage-biased junction, creating a pulse of current. We integrate the pulse and obtain the total charge that tunnelled. By calibrating the detector with photons of known energy, we determine the transfer function between the incident energy and the output charge. We can then use the transfer function for doing spectrometry on photons of unknown energy within the calibrated range.

The choice of the absorber material depends on the energy range of the photons. We want the material to be mainly absorbing, instead of being reflective or transparent, in that energy range. In this work we are developing spectrometers for detecting photons in

the optical / UV range. A very good choice in this range is Ta, which has a reflectivity around 40% in the $2-12$ eV range for a thick sample [Weaver1974] (to avoid transmission of photons through the material). This means that approximately 60% of the incoming photons are absorbed, the rest being reflected.

The absorber is in its superconducting state. In a superconducting metal, electrons with opposite wave vectors (**k**, -**k**) and opposite spins ($\uparrow$, $\downarrow$) are bound into pairs known as Cooper pairs. The Cooper pairs form a condensate which is the BCS superconducting ground state [BCS1957]. Excitations of the superconducting ground state, called quasiparticles, were calculated in 1958 by Bogoliubov and Valatin. The energy E_k of a quasiparticle with momentum $\hbar k$ is $E_k = \sqrt{\xi_k^2 + \Delta^2}$. Here ξ_k is the energy of a free electron with momentum $\hbar k$ relative to the Fermi energy E_F, thus $\xi_k = \frac{\hbar^2 \mathbf{k}^2}{2m} - E_F$. Figure 2.1 shows the quasiparticle energy as a function of free electron energy. There are two quasiparticle branches: the hole-like quasiparticles ($\mathbf{k} < \mathbf{k}_F$) and the electron-like quasiparticles ($\mathbf{k} > \mathbf{k}_F$). Each excitation is a superposition of a hole-like and electron-like quasiparticle. When a photon of energy larger than twice the energy gap, 2Δ, is absorbed in a superconductor, it breaks Cooper pairs and creates quasiparticle excitations.

The absorber must transfer the excitations to the tunnel junction quickly and efficiently (without losses). Previous work in our group showed this is possible with a clean Ta / Al interface [Gaidis1994]. The quasiparticles created in the Ta absorber then get 'trapped' in the lower-energy gap Al, and they tunnel across the junction. The trapping time is due to inelastic scattering of quasiparticles with phonon emission. For energies E that are large compared to the energy gap Δ, the scattering rate is proportional to $\left(\frac{E}{\Delta}\right)^3$. Quasiparticles with energies higher than $3\Delta_{Al}$ scatter down to lower energies in several tens of nanoseconds [Segall2000]. As long as the size of the Al trap is large enough that the diffusion time inside it is greater than the inelastic scattering time, the quasiparticles will not diffuse back to the Ta. Due to the different fabrication technique of our devices, the diffusion time from the Ta absorber into the Al trap in our first designs was comparable to the trapping

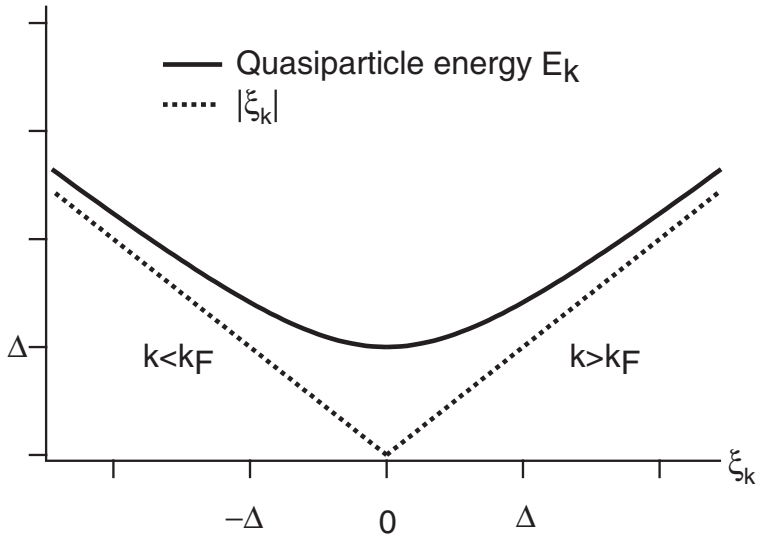

Figure 2.1: Quasiparticle energy E_k and ξ_k as a function of the free electron energy relative to the Fermi energy.

time, and the excitation transfer from the Ta absorber to the Al sensor was not efficient.

We therefore developed a new design which employs the Al electrodes of the junction as the absorber. In the $2-12$ eV region, Al has a reflectivity greater than 85% [Ehrenreich1963]. This means that most of the photons in this energy range will be reflected. It is only the absorbed photons that we aim to detect. We realize that this new design does not provide an efficient detector, but it allows us to study the physics of the detection process.

The energy down-conversion in a superconductor following the absorption of a photon with energy larger than twice the superconductor energy gap, Δ, is a complex process [Kozorezov2000]. The absorbed photon initially transfers its energy to a photoelectron. The energy down-conversion process is dominated at this stage by strong electron-electron interactions. Thus, the energy is shared among strongly interacting electrons. Once the average electron energy is comparable to the Debye energy, the electron-phonon inelastic scattering becomes stronger than the electron-electron inelastic scattering. The energy

down-conversion process releases a large number of phonons, which in turn excite more quasiparticles. A phonon of energy $\Omega > 2\Delta$ breaks one Cooper pair and creates two quasiparticles. A quasiparticle of energy $E > 3\Delta$ can emit phonons of energy $\Omega > 2\Delta$. Phonons of energy $\Omega < 2\Delta$ cannot break a Cooper pair, and quasiparticles with energy $E < 3\Delta$ cannot emit phonons with energies $\Omega > 2\Delta$, so neither contribute to the increase of the number of excess quasiparticles.

The mean energy ε needed to produce an excess quasiparticle [Kurakado1982] in Al is $\varepsilon = 1.7\Delta$ [Kozorezov2000], for an incident radiation with energy larger than several eV. This means that 60% of the absorbed photon energy goes into the quasiparticle system, while the remaining goes into phonons with energies below 2Δ. In a superconductor the gap energy Δ (of order meV) is much smaller than the Debye energy $\hbar\omega_D$ (tens of meV). The high characteristic energy of the phonons relative to the energy gap 2Δ plays an important role in the efficient transfer of energy from an absorbed photon to quasiparticle excitations. The phonons have enough energy to break Cooper pairs and generate excess quasiparticles, so that ε is not much larger than Δ. This is unlike in semiconductors, where the photon creates a single electron-hole excitation.

2.1.2 Quasiparticle Tunnelling

If we bias the junction with a bias voltage V_b, the quasiparticles will either tunnel directly, with an energy gain eV_b, or will reverse tunnel, losing eV_b of energy. The direct tunnelling processes allow quasiparticles to tunnel as electrons from left to right, or as holes from right to left (backtunnelling), as depicted in Figure 2.2. The reverse tunnelling processes allow quasiparticles to tunnel as holes from left to right, or as electrons from right to left. Table 2.1 shows the charge transfer for all the four processes. Reference [Tinkham1972] provides a clear description in terms of the BCS theory.

We can compute the tunnelling current and tunnelling rates associated with each of these processes [Golubov1994] using a simplifying approximation. We assume that the

Process #	Process type (process name)	Charge added on the right (in units of |e|)
1	direct (direct tunnelling)	-1
2	reverse (reverse tunnelling)	+1
3	direct (backtunnelling)	-1
4	reverse (reverse backtunnelling)	+1

Table 2.1: Tunnelling Processes

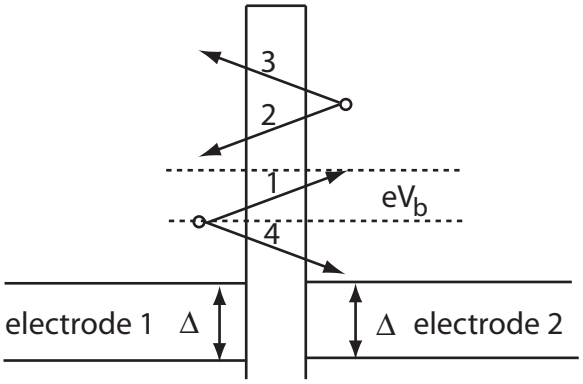

Figure 2.2: Different tunnelling processes shown in the modified excitation representation. The quasiparticles in the two electrodes are shown at energies higher the energy gap, for graphic simplicity.

two quasiparticle branches are symmetric and in equilibrium at an effective temperature $\ll T_C$, and that their currents can be added independently. We also assume the two electrodes are at the same temperature T. (There are special cases when the currents from the two degenerate channels of hole-like and electron-like quasiparticles can not just be summed up. This occurs in the Tomasch effect [Tomasch1966], when the interference between the two channels creates a current which varies with voltage [McMillan1966], and also in the charge-imbalance regime, when the **k** states below and above the Fermi surface at $\mathbf{k}_F$ are not equally populated and therefore their occupation numbers cannot be described by the Fermi function of thermal equilibrium.)

Using this approximation, we can write the direct/reverse tunnelling particle current from electrode 1 to electrode 2. The quasiparticles start at an initial energy E, gaining energy eV_b if they tunnel as electrons (direct tunnelling), or losing energy eV_b if they

tunnel as holes (reverse backtunnelling):

$$I_{1\to 2}(E \to E \pm eV_b) = \frac{2\pi}{\hbar} \mid M \mid {}^2 N_1(E) f_1(E) N_2(E \pm eV_b)[1 - f_2(E \pm eV_b)] \tag{2.1}$$

where M is the tunnelling matrix element between the two states, N(E) is the superconducting density of states, and f(E) is the Fermi function. The number of occupied initial quasiparticle states in electrode 1 is $N_1(E)f_1$. The quasiparticles can only tunnel into the empty states at the respective energies from the second electrode, $N_2(E \pm eV_b)[1 - f_2(E \pm eV_b)]$.

The tunnelling times can be computed from the tunnelling current:

$$\tau^{-1}_{tunn1\to 2}(E \to E \pm eV_b) = \frac{I_{1\to 2}(E \to E \pm eV_b)}{N_1(E) f_1(E)} \tag{2.2}$$

where $N_1(E)f_1(E)$ is the number of quasiparticles available to tunnel from the first electrode.

To compute the total tunnelling current, one has to integrate (2.1) over the available energy range of E. We assume that the density of states in a normal metal is constant within millielectronvolts (meV) of the Fermi energy, which is on the order of a few electronvolts (eV). The superconducting density of states then is:

$$N_{1,2}(E) = \begin{cases} \dfrac{N_n(0)E}{\sqrt{E^2 - \Delta^2}} & E > \Delta \\ 0 & E < \Delta \end{cases} \tag{2.3}$$

where $N_n(0)$ is the normal metal density of states at the Fermi level and Δ is the superconducting energy gap.

The total electrical tunnelling current is computed as the sum of all the tunnelling processes in the junction, considering the sign of the charge transferred (Table 2.1). The direct tunnelling and the backtunelling processes contribute positive currents, while the reverse tunnelling and the reverse backtunnelling contribute negative currents. Promoting direct backtunnelling is a technique first used by N. E. Booth [Booth1987] to increase the effective charge created by a photon.

$$I_{dc}^{electrical} = I_{1\to 2}^{direct} - I_{1\to 2}^{reverse} + I_{2\to 1}^{backtunnel} - I_{2\to 1}^{revbacktunnel} \tag{2.4}$$

In the low temperature limit $k_BT \ll \Delta$ and in the subgap biasing region $eV < 2\Delta$, the subgap current is estimated to be [VanDuzer1981]:

$$I_{dc}^{electrical} = \frac{2(eV+\Delta)}{R_n} e^{-\Delta/k_BT} \sqrt{\frac{2\Delta}{eV+2\Delta}} sinh\left(\frac{eV}{2k_BT}\right) K_0\left(\frac{eV}{2k_BT}\right) \tag{2.5}$$

where R_n is the normal state resistance of the junction, and K_0 is the zeroth-order modified Bessel Function.

The quasiparticle tunnelling times for direct/reverse processes taking them from an energy E in the first electrode to an energy $E \pm eV$ in the second electrode are:

$$\tau_{tunn1\to2} = 2e^2 N_n(0) R_n Vol_1 \frac{\sqrt{(E \pm eV)^2 - \Delta^2}}{E \pm eV} \tag{2.6}$$

where Vol_1 is the volume of the electrode the quasiparticles are tunnelling from.

For the normal state, the times corresponding to an electron tunnelling from electrode 1 to 2 is:

$$\tau_{tunn1\to2} = e^2 N_n(0) R_n Vol_1 \tag{2.7}$$

2.1.3 Quasiparticle Recombination

If quasiparticles get lost before tunnelling, they do not contribute to the signal and the detector energy resolution is degraded. An important loss mechanism is quasiparticle recombination. The number of ways N quasiparticles can be paired up is $\frac{1}{2}N(N-1)$, which in the case of a large N can be approximated by $\frac{N^2}{2}$.

We define R to be the recombination rate per unit density of quasiparticles. Since each recombination event removes 2 quasiparticles, the recombination rate τ_{rec}, not taking into account any quasiparticle generation, can be computed from:

$$\frac{\partial N}{\partial t} = -N(N-1)\frac{R}{Vol} \approx -N^2 \frac{R}{Vol} \tag{2.8}$$

$$\frac{\partial N}{\partial t} = -\frac{N}{\tau_{rec}}, with\ \Gamma_{rec} = \frac{1}{\tau_{rec}} = \frac{NR}{Vol} \tag{2.9}$$

The intrinsic recombination lifetime of low energy quasiparticles in superconductors nearly in thermal equilibrium has been calculated by [Kaplan1976]. The leading low-temperature behavior is:

$$\tau_{rec,eq}^{-1} = \frac{1}{\tau_0}\pi^{\frac{1}{2}}\left(\frac{2\Delta}{k_B T_C}\right)^{5/2}\left(\frac{T}{T_C}\right)^{1/2} e^{-\Delta/k_B T} \tag{2.10}$$

where τ_0 is a constant dependent on the material that reflects the strength of the electron-phonon interaction. For Al τ_0 was found to be 0.438 μs [Kaplan1976].

The thermal number of quasiparticles, N_{th}, in a superconductor at a temperature $T \ll T_C$ and having a Fermi distribution is calculated by integrating the BCS density of states and is found to be:

$$N_{th} = N_n(\varepsilon_F) Vol \sqrt{2\pi\Delta k_B T} e^{-\Delta/k_B T} \tag{2.11}$$

In Figure 2.3 we show the density of thermal quasiparticles for different values of the gap as a function of temperature. We can see how for the same temperature, the thermal energy excites fewer quasiparticles in the higher energy gap materials.

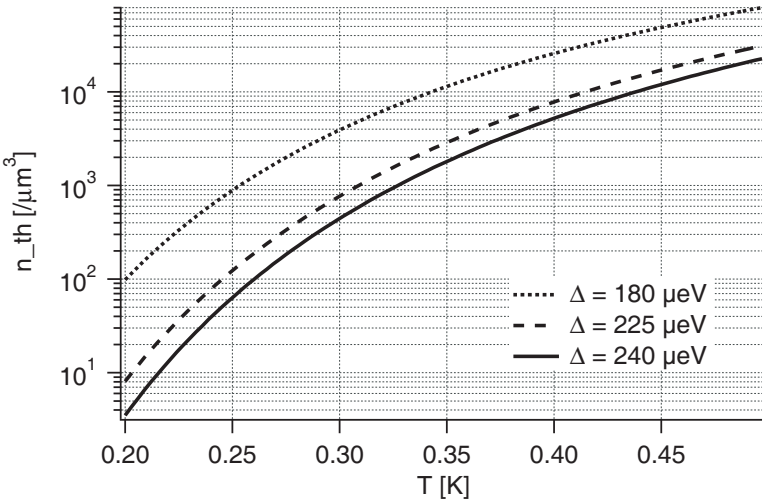

Figure 2.3: Quasiparticle density as a function of temperature for materials with different energy gaps.

By using Kaplan's recombination time near equilibrium and the thermal number of quasiparticles in (2.9), we can extract the recombination constant R:

$$R = \left(\frac{2\Delta}{k_B T_C}\right)^3 \frac{1}{2N_n(\varepsilon_F)\tau_0\Delta} \tag{2.12}$$

For clean aluminum (with $\Delta = 180\,\mu$eV, $T_C = 1.2$ K), with $N_n = 1.5 \times 10^{47}\,J^{-1}\,m^{-3}$ [Kittel] and τ_0 from [Kaplan1976], R has the value of 11.1 μm^3/s.

The recombination rate depends on temperature via the thermal background. In Figure 2.4 the recombination time Γ_{rec}^{-1} when there are no excess quasiparticles is plotted versus temperature for different values of the energy gap.

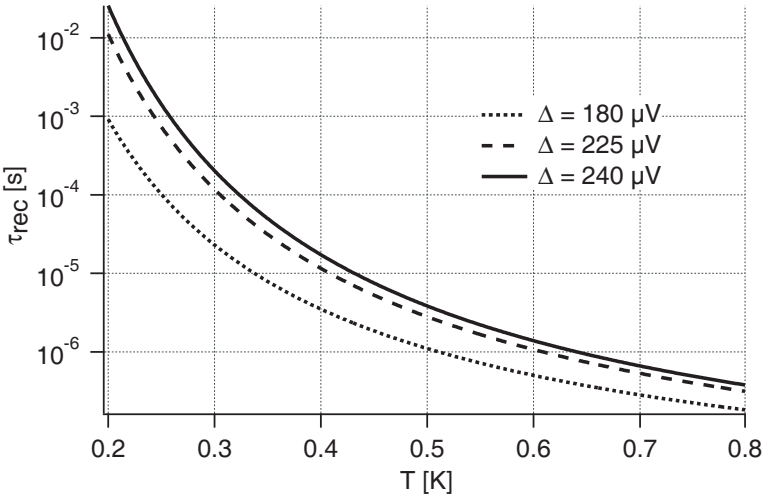

Figure 2.4: Recombination time as a function of temperature for different values of the energy gap Δ.

After a photon has been absorbed, there are N_{excess} excess quasiparticles. By applying (2.8) and (2.9) to the recombination of excess quasiparticles, we obtain:

$$\frac{\partial N_{excess}}{\partial t} = -(N_{excess}^2 + 2N_{excess}N_{th})\frac{R}{Vol} \tag{2.13}$$

The term containing the square of the thermal number of quasiparticles, which is not shown in (2.13), is cancelled by thermal generation. The first factor in equation (2.13) is due to the self-recombination of the excess quasiparticles, while the second one is due to the recombination of the excess quasiparticles with the thermal ones.

We have to remember that during the relaxation in energy of the initially created high-energy quasiparticles, a hot-spot will be created in the absorber where the effective temperature is much higher than the bath temperature. We should even be careful about de-

scribing the system in terms of an effective temperature. In the hot-spot volume the faster recombination rate would create a loss mechanism for the initial quasiparticles.

Extracting the intrinsic quasiparticle lifetime is complicated in most experiments by the phonon-trapping effect [Rothwarf1967]. Due to the acoustic mismatch between the superconducting film and the substrate, a certain fraction of the phonons with energies larger than 2Δ will be reflected back into the film, continuing to break pairs and to create excess quasiparticles, thus prolonging the effective recombination lifetime.

2.2 Diffusion Engineering

There are different approaches for achieving intrinsic charge multiplication from the excess quasiparticles in an STJ, such as gap-engineering and diffusion-engineering. Gap-engineering involves having the two superconducting electrodes make electrical contact on each side of the junction to higher-gap superconductors, as in Figure 2.5b. Figure 2.5a shows the energy band diagram for a gap-engineered device. In this case the charge multiplication factor depends on the ratio of the two energy gaps, the tunnelling and backtunnelling times, the energy relaxation rate in the electrodes, and the quasiparticles' lifetime. Diffusion-engineering uses a higher-gap material on only one side of the junction. The confinement of the quasiparticles on the other side of the junction is controlled by a long and narrow wire termination, as seen in Figure 2.5d. The energy band diagram in this case is shown in Figure 2.5c. The wire acts as a constriction that slows down the diffusion of the excess quasiparticles. If the dwell time around the junction in the counterelectrode is longer than the backtunnelling time, the quasiparticles will backtunnel, effectively increasing the current in the same direction as the direct tunnelling current. If the quasiparticles relax in energy before they tunnel, the reverse tunnelling and the reverse backtunnelling processes are avoided.

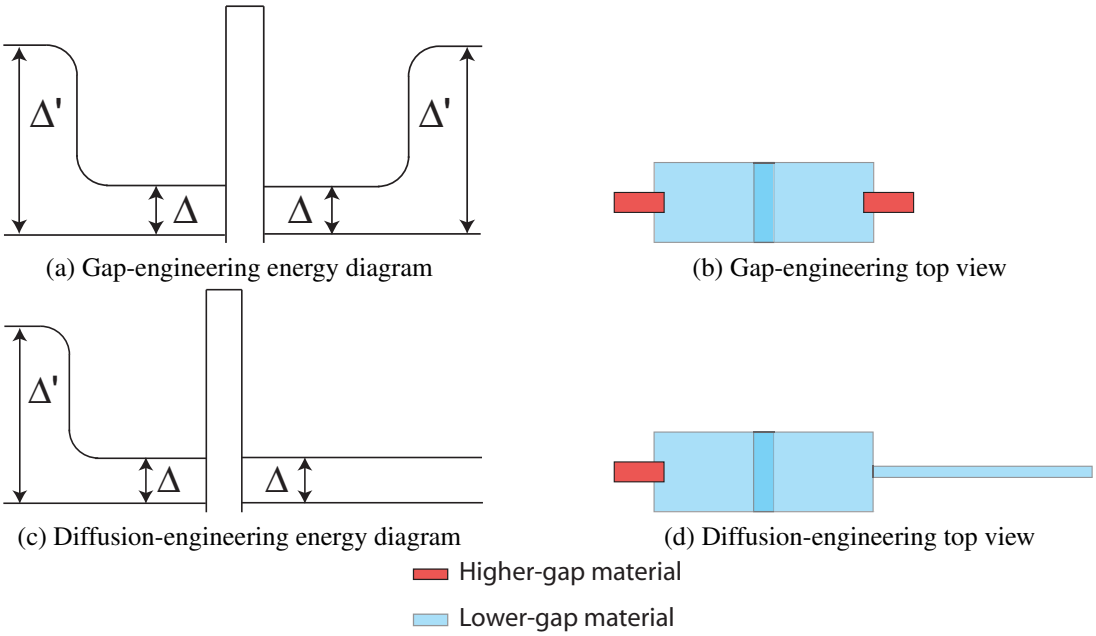

Figure 2.5: Energy diagram for devices employing different intrinsic charge multiplication techniques. The tunnel junction is between the two lower-gap electrodes.

2.2.1 Diffusion

In our simulations we will only consider a two-dimensional diffusion process. This is a very good approximation for two reasons:

1. The thickness of our films (0.120 μm) is much smaller than the lateral sizes of our detector ($5 \times 10\ \mu m^2$ per electrode).

2. The diffusion time over the thickness of each electrode of the junction is much smaller than the other time scales relevant to our system. For D $= 8\ cm^2/s$ we obtain a diffusion time of 18 ps over the 120 nm thickness, while the tunnelling times are on the order of 5 μs.

The 2D diffusion equation describes the statistical movement of randomly moving particles in two dimensions. Each particle obeys Brownian motion, as described by a random walk. The diffusion equation captures the temporal and spatial evolution of the probability distribution n(x,y,t) of having at time t an average particle density n at point (x,y). The two-dimensional diffusion equation with no loss is:

$$\nabla^2 n - \frac{1}{D}\frac{\partial n}{\partial t} = 0 \tag{2.14}$$

where D is called the diffusion coefficient. Solving this linear partial differential equation for an infinite plane, in Cartesian coordinates, one obtains:

$$n(x,y,t) = \frac{1}{4\pi Dt} e^{\frac{-(x^2+y^2)}{4Dt}} \tag{2.15}$$

which in polar coordinates is:

$$n(x,y,t) = \frac{1}{4\pi Dt} e^{\frac{-(r^2)}{4Dt}} \tag{2.16}$$

This is just a normalized Gaussian function that spreads out in time with a speed that depends on the diffusion constant.

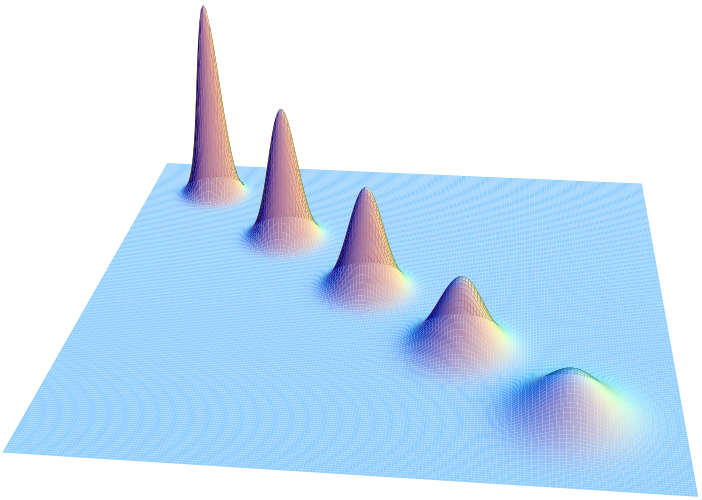

Figure 2.6: Time evolution of a Gaussian function subject to diffusion and center of mass motion.

Solving the equation becomes more complicated when one introduces boundary conditions and an additional term describing the quasiparticle lifetime. Two types of boundary conditions describe our system:

1. Dirichlet boundary conditions, specifying the value of the distribution function on a line, and

2. Neumann boundary conditions, specifying the normal derivative of the distribution function on a line.

2.2.2 Simple Analytical Model

The geometry of the counter-electrode and out-diffusion lead is shown in Figure 2.7. We can obtain an analytical solution for the concentration of quasiparticles if we make a few assumptions allowing us to use the 1D diffusion equation. In the next paragraphs, the relevant time scales are those set by tunnelling, backtunnelling and outdiffusion:

1. We have to assume that the density of quasiparticles becomes uniform within the absorber on a time scale $\tau_{uniform}$ much shorter than the other relevant time scales. Afterwards, the quasiparticle density in the counter-electrode will be spatially constant. This way we can compute the number of quasiparticles in the counter-electrode at any time t as the concentration n(t) times the volume of the counter-electrode.

2. The area of the counter-electrode has to be much larger than the area of the wire, with the width of the wire much smaller than its length (1D assumption).

3. The time it takes the wire to reach a quasiparticle concentration that is linear in x is much shorter than the other relevant time scales. If $LW \gg wl$, this requirement is equivalent to the requirement that l^2/D be much less than the decay time for n(t) in the counter-electrode.

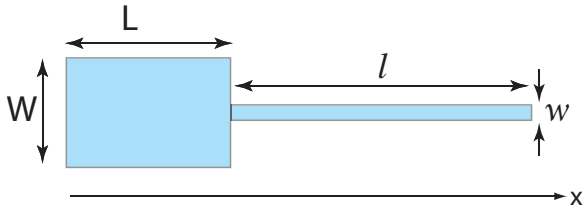

Figure 2.7: Geometry of the counter-electrode and out-diffusion lead in our detectors.

Given the above assumptions, we can solve for time evolution of the total number of quasiparticles. We start by invoking Fick's First Law of Diffusion, which states that the flux of particles is proportional to the gradient of their density:

$$flux = (-D)\frac{dn(x)}{dx} \tag{2.17}$$

From the continuity equation, we know that summing up the particle flux flowing out of the volume gives us the time rate of decrease of the total number of quasiparticles N_{tot}. Assuming a uniform flux of quasiparticles along the width w of the lead, we obtain:

$$flux \times w \times d = \frac{dN_{tot}}{dt} \tag{2.18}$$

By combining (2.17) and (2.18) we can write:

$$\frac{dN_{tot}}{dt} = (-D)\frac{dn(x)}{dx} wd \tag{2.19}$$

In the narrow wire the concentration profile is linear, extending from the spatially constant concentration in the counter-electrode down to zero, at the superconductor / normal metal interface. From Figure 2.8 we can write down:

$$\frac{n(x+dx)-n(x)}{dx} = \frac{n(L)}{l} = sec\theta \tag{2.20a}$$

$$\frac{dn(x)}{dx} = \frac{n(L)}{l} \tag{2.20b}$$

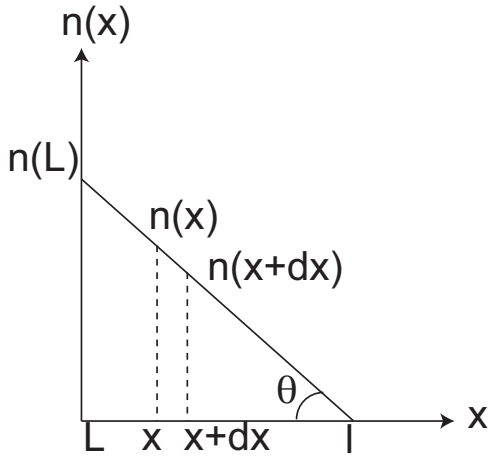

Figure 2.8: Linear quasiparticle concentration profile in the wire.

The total number of quasiparticles can be written as $N_{tot} = n(L) \times d \times (LW + 0.5lw)$, due to the linear profile in the lead. Combining (2.20b) and (2.19) we get:

$$\frac{dN_{tot}}{dt} = -\frac{DwN_{tot}}{l(LW + 0.5lw)} \tag{2.21}$$

The solution to the equation (2.21) has the form $N_{tot}(t) = N_0 \times exp(t/\tau)$, with τ given by:

$$\tau = \frac{1}{D}\frac{l}{w}(LW + 0.5lw) \tag{2.22}$$

2.2.3 Electrical Equivalent

We can think of the one-dimensional problem in terms of an electrical circuit model. The counter-electrode acts as a reservoir of quasiparticles, which are discharged through the out-diffusion lead. Therefore we can model the counter-electrode as a capacitor whose capacitance is proportional to its total area, $C_{CE} \propto LW$. If the tunnelling time is much shorter than the recombination time in the counter-electrode, $C_{CE} = LW$. The lead acts as a two-dimensional resistor where the diffusion coefficient D replaces the conductivity σ. The three-dimensional formula for resistance $R = \frac{l}{\sigma A}$, with A the transverse area of the resistor, thus becomes $R_{lead} = \frac{l}{Dw}$. Besides playing the role of a resistor, the lead also has some associated capacitance, similar to stray capacitance in a circuit. We can think about the capacitance in terms of the charge (quasiparticles) stored in the lead, yielding $C_{lead} = 0.5lw$.

Figure 2.9 shows the RC electrical model. The time constant $\tau = RC$ for this circuit comes out to be equation (2.22). We have not included quasiparticle losses due to quasiparticle recombination so far in this discussion.

2.2.4 Diffusion Simulation

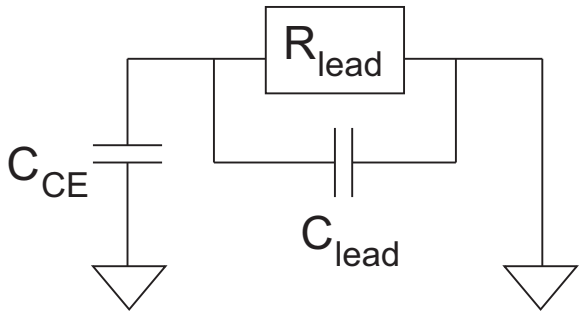

Figure 2.9: Electrical circuit model for a diffusion-engineered device.

Although the simple analytical model presented above provides a good first approximation to be used in our device design, it does not contain the full picture of the diffusion process. To get a better understanding of the diffusion process, we use Matlab's Partial Differential Equation (PDE) Toolbox to solve the parabolic diffusion equation in two dimensions:

$$d\frac{\partial n}{\partial t} - \nabla(D\nabla n) + an = f \tag{2.23}$$

with n being the quasiparticle density. In our case $d = 1$, D is the diffusion constant, a is a loss term modelled as τ_{rec}^{-1}, and f is a drive term that is zero.

We use two different types of boundary conditions (b.c.), as seen in Figure 2.10. We have Neumann boundary conditions on all sides except the end side of the wire. The Neumann b.c. sets the normal component of the quasiparticle flux. In our case this is zero since the quasiparticles cannot leave the boundaries except through the end of the wire. At the end of the wire there is contact to a normal metal or a very large area superconductor, where there are no excess quasiparticles. For this boundary we have Dirichlet type b.c., setting the distribution function to zero.

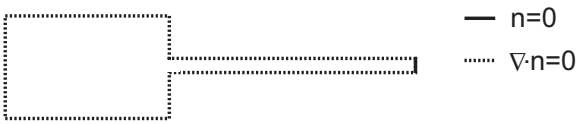

Figure 2.10: Dirichlet and Neumann boundary conditions set on our domain.

No other loss mechanism is taken into account in our simulation. The two-dimensionality of our problem is valid as long as the thickness of our layers is much smaller than the smallest geometrical feature in our design, the wire width. In practice, the total layer thickness is 0.12 μm, while the wires are as narrow as 0.25 μm. We can still use the results with the caveat that the quasiparticles will take shorter than the simulated time to out-diffuse down the wire. Effectively, the third dimension (thickness) can be folded into a larger second dimension (width).

The input simulation parameters are:

• the diffusion constant D [cm^2/s],

• the electrode and wire dimensions W, L, w, l [μm],

• the quasiparticle initial spike position and the total number of quasiparticles in the spike,

• the loss time,

• the time range for which the simulation should be run [μs] and the time resolution [ns/frame], and

• the percentage of quasiparticles left.

We monitor three regimes, recording the time at which each starts. In chronological order, we have:

• uniformity - the time after which the density of quasiparticles reaches uniformity in the electrode,

• linearity - the time after which the quasiparticle density profile becomes linear in the lead (this is also the steady state solution for our system),

• percentage reached - the time after which the desired percentage of quasiparticles is left in our system.

After the system reaches linearity, the total number of quasiparticles in the system at each point in time can be calculated easily. Since in the electrode the concentration is spatially constant $n(L)$ and in the wire it is linear from its value in the electrode down to

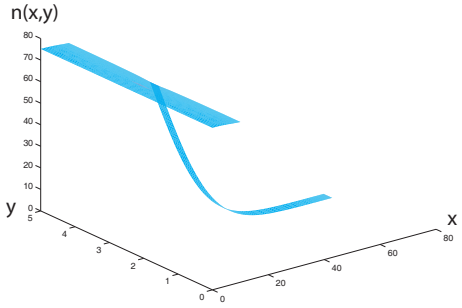

(a) Quasiparticle concentration in the counter-electrode becomes uniform.

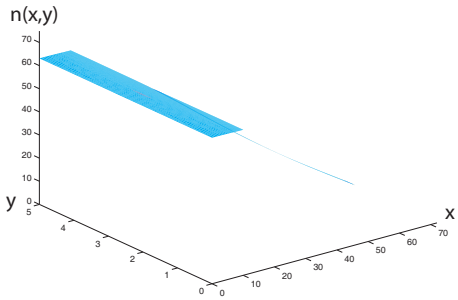

(b) Quasiparticle concentration in the lead becomes linear.

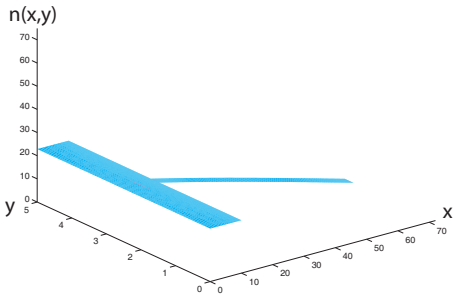

(c) 33% of quasiparticles have diffused out the lead

Figure 2.11: Evolution in time of the quasiparticle concentration in the counter-electrode and lead. The initial number of excess quasiparticles is 4000, the electrode area is $5 \times 10\ \mu m^2$, and that of the wire is $0.25 \times 62\ \mu m^2$.

zero, the total number is $N_{tot} = n(L) \times (LW + 0.5lw)$. This is the regime for which our simple $1D$ model was valid, but now we have the $2D$ version of it.

The simulations have been done with the same initial number of 4000 quasiparticles and a time resolution of 100 ns unless otherwise stated.

Uniformity

With a diffusion constant of 8 cm^2/s, it takes under 10 ns for the initial hot spot of quasiparticles to spread out uniformly within the $5 \times 10\ \mu m^2$ area of our electrode. For as slow a diffusion as 2 cm^2/s, an area of $5 \times 10\ \mu m^2$ becomes uniformly filled in less than 200 ns. So for any practical cases , the uniformity time scale is very short compared to the microsecond timescales of the other relevant processes.

Linearity

The time $\tau_{linear\_simulation}$ to reach the linear regime in the lead depends on many parameters. In Figure 2.12 we show the variation with the diffusion constant. As expected, this time increases as the quasiparticles diffuse more slowly. We can vary the value of the Al diffusion constant from $1 - 60 cm^2/s$, depending on the impurity concentration incorporated in the film.

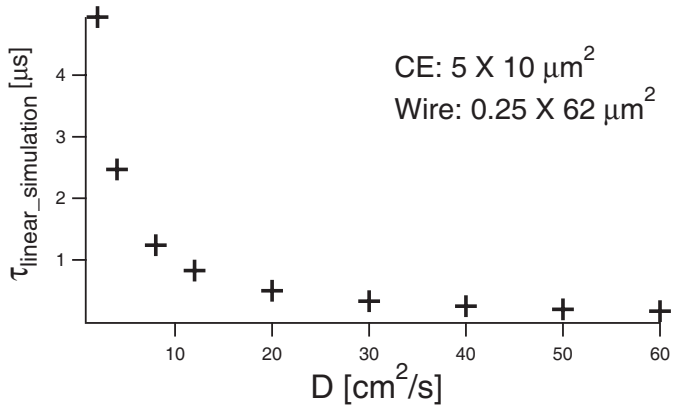

Figure 2.12: Variation of the time for the concentration profile in the wire to become linear with diffusion constant.

Out – diffusion

In Figure 2.13 we compare the time obtained from the simulation to the time obtained from using the linear regime formula. The simulation time was computed as the time after which 36% of the initial number of quasiparticles are left in the electrode and wire. As input parameters we used diffusion constants from 2 cm^2/s up to 60 cm^2/s, a counter-electrode of $5 \times 10\ \mu m^2$, a lead of $0.25 \times 62\ \mu m^2$, and a loss time of $150\ \mu s$.

We notice the deviation from the linear regime formula as the out-diffusion time gets longer. The linear regime formula $\tau_{out\_formula}$ overestimates the out-diffusion time obtained from the simulation, $\tau_{out\_simulation}$. This effect becomes more relevant for the slower diffusion cases, i.e. for the smaller diffusion coefficients, reaching a discrepancy of about 30%. This is due to quasiparticle recombination losses, which become more significant at longer times.

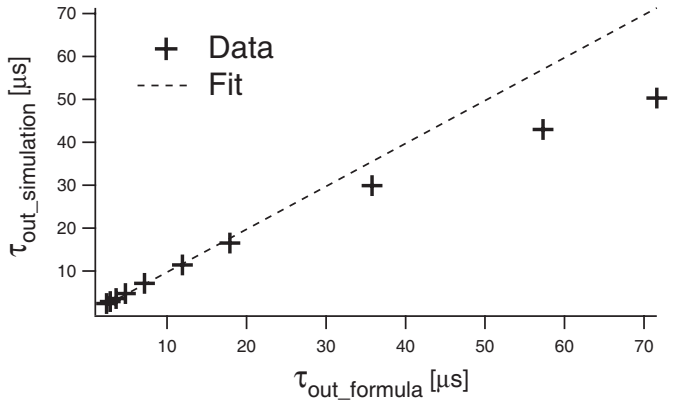

Figure 2.13: Fit with a slope of 1 for times up to 20 μs of the simulation time versus the time calculated with the linear regime analytical formula.

2.3 Diffusion Engineering Flowchart

In this section we examine the constraints we encounter in designing the diffusion-engineered devices and the relation between different parameters. This is presented schematically in Figure 2.14. We will investigate each parameter on the last rows of the chart and see how we can solve some of the associated conflicting requirements.

Our aim is to maximize the signal-to-noise ratio, S/N, in our detector. The signal is the collected charge, which is proportional to the charge multiplication factor p and the initial excess number of quasiparticles N_0 created by the absorbed photon. N_0 is a function of the energy gap of the absorber and the photon energy. The charge multiplication factor is the ratio of the out-diffusion time to the tunnelling time. In a single-tunnelling device p $= 1$, while in a diffusion-engineered device we want to be able to maximize p. The flowchart in Figure 2.14 has dashed lines going to the parameters that need to be minimized, and continuous lines going to the parameters that need to be maximized. We notice how some parameters need to follow opposite directions (be at the same time minimized and maximized) dictated by optimization of different parameters. For these cases an optimum value has to be achieved. In certain situations the direction of change for some parameters will not be the one indicated in the chart due to other constraints. I will explain each case.

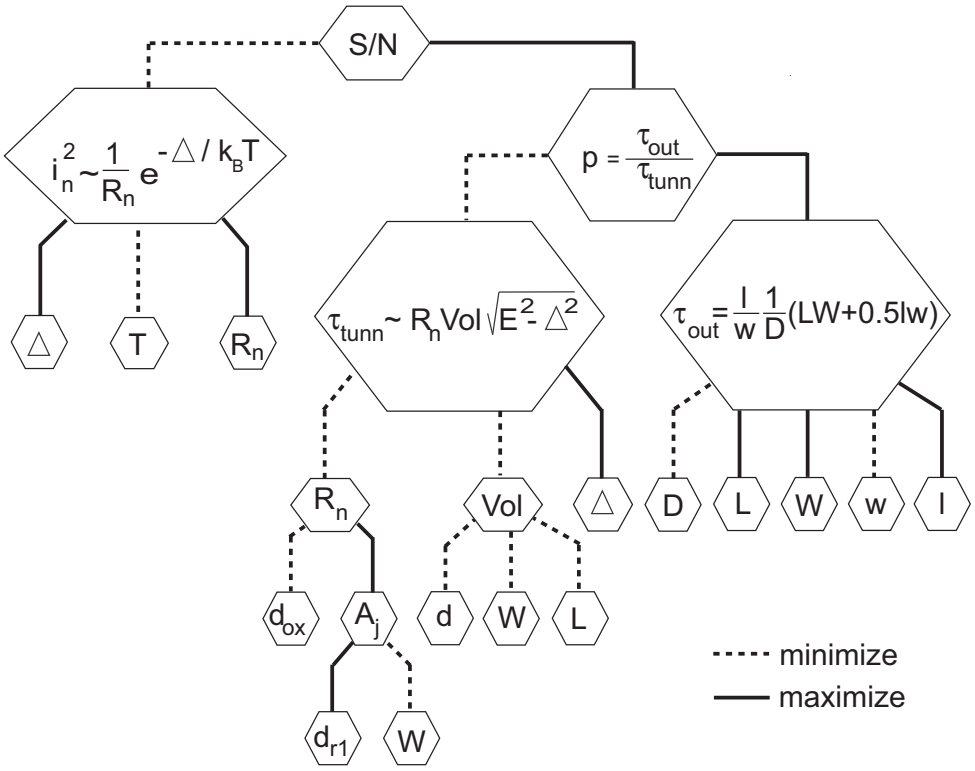

Figure 2.14: Diffusion engineering flowchart reflecting the different connections between device parameters.

Lowering the intrinsic device noise contribution also increases the signal-to-noise ratio of our measurements. The device intrinsic current noise is $i_n \sim \sqrt{I_{dc}}$. From equation (2.5) we see that both a lower working temperature and a higher normal resistance would have the desired effect. The higher normal resistance is achieved by making the junction area A_j smaller and by lowering the junction current density j_C; j_C is proportional to the junction's conductance and depends on the oxide barrier thickness d_{ox}. In practice there is a limit to the oxidation achievable without introducing an unacceptable amount of impurities. The lower limit is set by how uniformly one can achieve the thinnest oxide layer. In practice, for the Al junctions fabricated in our facilities, the critical current density j_C of the junction is limited to a range of $10 - 175\, A/cm^2$. If we want even smaller device current noise, we need to fabricate smaller junctions.

Previously we used an optical lithography tri-layer junction process followed by wet etch patterning, which limited our junction sizes to tens of squared microns, with no size

smaller than 7 μm. In practice, the lowest subgap current at 0.24 K was on the order of 1.5 nA. By switching to the Dolan bridge double-angle fabrication technique (as explained later in the fabrication chapter) we were able to fabricate junctions as small as $1 \times 5\ \mu m^2$. These smaller junctions have a much smaller current noise than larger junctions, if operated at the same temperature. Although smaller-size junctions would have even less current noise, their tunnel time would be much longer, possibly longer than the loss time in the device. One way to decrease the tunnel time while keeping the junction size small is to make the junction more transparent, i.e. with a higher j_C. However, high-transparency oxide barriers tend to develop superconducting shorts, where the non-uniformity of the oxide allows the two electrode layers to touch. This translates into a critical current that cannot be suppressed, making voltage-biasing the junction difficult and increasing the subgap current of the device. All our designs have $1 \times 5\ \mu m^2$ junctions. This allows us to go to a sub-gap current as low as 0.1 to 0.2 nA, a factor of 10 better than with the previous tri-layer process.

The tunnelling time has to be longer than both the quasiparticle energy relaxation time and the fastest time we can detect, which is set by our electronics bandwidth, and is on the order of a couple of microseconds. If we want a large charge multiplication factor, the diffusion time should be longer, limiting the detector's speed. So we decided that the mid-ground between these two conditions is a tunnel time of 5 μs.

With the tunnelling time decided from the above considerations and the maximum junction area set by the nature of the fabrication process, we had to adjust the oxidation time accordingly.

While for minimizing the tunnelling time we would want small electrode dimensions L and W, for maximizing the out-diffusion time these have to be made large. So we have to optimize the geometry using these constraints.

The width of the out-diffusion lead, w, has to be small. Its size is determined by how narrow we can reproducibly fabricate a uniform and long line. Non-uniformities can

influence the local energy gap value, possibly introducing undesired trap-centers in regions with lower gap. At the same time, the out-diffusion lead should be as long as possible.

The energy gap Δ can be increased by using a higher-gap material, achieved by using 'dirty' aluminum. We decided to continue using Al for our junctions, given the high yield and reliability of the fabrication process. What we refer to as 'dirty' aluminum is aluminum with an enhanced energy gap, achieved by deposition in an oxygen background. The 'dirtier' the aluminum, the higher the gap, meaning smaller grains that slow down the quasiparticle diffusion. So having higher gap aluminum was a requirement consistent with having a smaller diffusion constant D.

Chapter 3

Experimental Setup

3.1 Overview

In this chapter we present the setup used for our experiments. Much of the experimental apparatus was constructed by previous researchers at Yale, and it is described in detail in previous theses [Gaidis1994], [Friedrich1997], [Segall2000], [Li2002], [Wilson2002]. We shall emphasize those aspects that are new or modified. The experimental setup is schematically presented in Figure 3.1. The devices are mounted inside a cryostat with the base temperature of 0.24 K. A custom-made battery-powered electronics box is used to dc-bias the junction in the sub-gap region and to amplify the ac-current signal from the device. The cryostat and the electronics box are located in a bigger shielding box, which prevents electromagnetic interference. The pumping lines for the cryostat fit through a hole into the shielding box. The ac signal is further amplified and filtered outside of the shielding box before it is recorded on an oscilloscope. The data are downloaded via GPIB[1] to a computer, where they are later analyzed. The optical testing is done using an attenuated beam from an ultra-violet pulsed laser. The light is coupled from the laser to the device via optical fibers. An optically-synchronized electrical signal from the laser is used to trigger the data recording.

[1] General Purpose Interface Bus is an interface system that connects programmable instruments to their computers

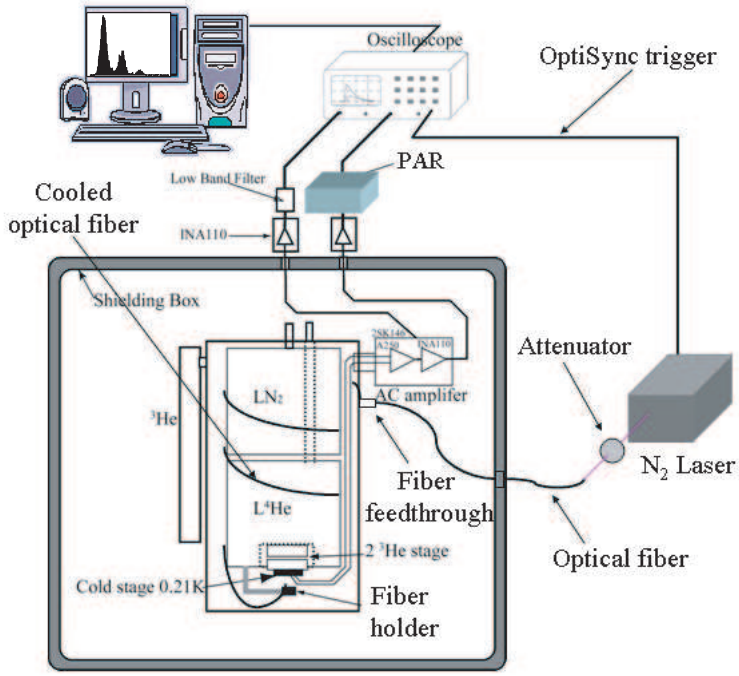

Figure 3.1: Experimental setup.

3.2 Cryogenics

For testing our devices at cryogenic temperatures we use a custom-made, two-stage, pumped ^{3}He dewar, known as Tiny Tim. It has a liquid N_2 stage, a liquid ^{4}He stage and two closed-cycle ^{3}He pots. The stages are nested into each other, and all the pumping lines and contacts for the second ^{3}He pot are pre-cooled through the first one. Inside the ^{4}He stage there are two charcoal absorption pumps for the two pots. The copper cold finger is connected to the second pot, allowing the base temperature to reach 0.24 K.

We start the cool-down procedure by pumping out the dewar with a turbo pump, outside the shielding box. We wait for the pressure to drop down to 10^{-4} Torr, which takes about 7 hours. While still pumping, we pre-cool both the N_2 and the ^{4}He tanks with liquid N_2. It takes a minimum of 3 hours for the temperature to come down to 77 K, but we usually leave the liquid N_2 in overnight. We remove the liquid nitrogen from the helium tank with pressurized helium gas, making sure no liquid is left in the tank. We stop pumping

on the dewar just before transferring liquid ^{4}He into the ^{4}He tank. The ^{4}He stage reaches 4 K in about half an hour, after which we top it off with more helium. The dewar is then transferred into the shielding box and we start pumping on the liquid ^{4}He. In about 20 minutes the base temperature reaches 1.5 K, which is low enough to start condensing the ^{3}He. We open valves from the pressurized room temperature ^{3}He cylinder attached to the side of the dewar, allowing the ^{3}He to condense into the two pots. Full condensation is attained in one hour. The condensed ^{3}He pots are thermally disconnected from the ^{4}He stage and the charcoal absorption pumps are instead thermally connected to it. The cold charcoal starts absorbing the vapors on top of the condensed ^{3}He, lowering the pressure and therefore its temperature. The base temperature is reached in about 2 hours and lasts for the next 6 hours. The first stage is cooled to about 0.3 K. The second stage is cooled to 0.24 K through a pumping line cooled through the first stage.

Half an hour before taking data we start pumping with a turbo pump on the liquid N_2 tank. Lowering the temperature makes the nitrogen slushy, preventing it from 'bubbling'. Without this precaution, there were mechanical vibrations from the nitrogen bubbles which used to be picked up as electrical noise by the wiring leading to our samples. Freezing the nitrogen in this fashion solved the problem.

At the end of the experiment we stop pumping on both the nitrogen and the helium, we thermally reconnect the ^{3}He pots to the ^{4}He bath, and we open the valves that allow the ^{3}He to evaporate into the ^{3}He room temperature cylinder. To prevent water condensation inside the cryostat, we do not open the dewar for at least 12 hours.

3.3 Electronics

3.3.1 Electrical Contacts

In early experiments the contact from the device's contact pads to the 0.2 K stage wires was done using Pogo pins from Emulation Technology, Inc. After 08/18/2004, we decided to change the contact technique for two reasons: first, the new devices are fabricated using

only e-beam lithography, so macroscopic 1×5 mm contact pads for the pogo pins would take a long time to pattern; second, the pogo pins had a limited and relatively short lifetime if thermally-cycled many times, the main failure mode being becoming open only at low temperatures. The new contact technique uses wire-bonding. The bonding is easily done with Al wire from patterned 150×400 μm Au pads onto 0.75 cm wide Cu traces. The traces, deposited on top of a circuit board piece, connect to a 20-wire ribbon cable. Since the cryostat has only 12 wires available, the 8 unused wires from the ribbon cable were cut short and left unconnected. The chip with the device is glued down with GE varnish[2] to a Cu pad located roughly in the middle of the circuit board piece. The Cu pad insures a better thermal contact to the 0.2 K cold finger. The circuit board piece is placed in good thermal contact with the cold finger via a thin layer of Apiezon N thermal grease.

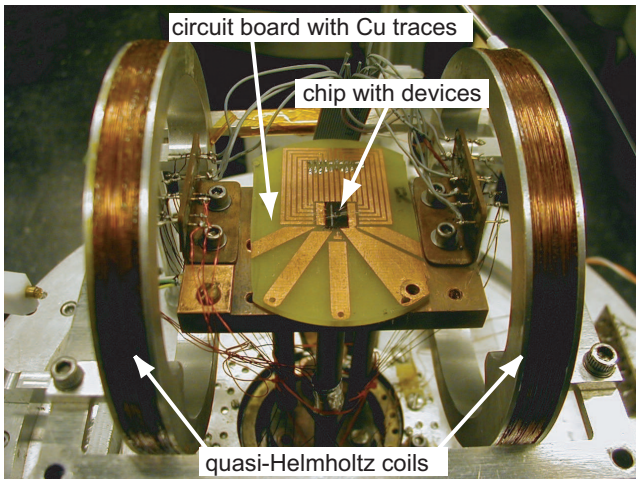

Figure 3.2: Circuit board with Cu traces and wire-bonded devices on a chip, along with the quasi-Helmzoltz coils used to produce a parallel magnetic field.

[2]GE varnish 7031 is an adhesive and electrical insulator, usually used when good thermal contact is desired.

3.3.2 DC Electronics

The 12 wires are tightly wrapped around the several cold stages before being connected via a hermetic military connector outside the dewar to an electronics box. The electronics box supports two dc lines, for monitoring the devices' dc bias point (voltage and current), and one ac line, for recording the device's ac current response. The dc-bias circuitry and the first stage of the ac amplification chain are located on a printed circuit board (PCB), in a $18 \times 12 \times 8$ cm^3 metal box. In order to minimize the 60 Hz interference from the power lines, the amplifiers and voltage regulators on the PCB are powered solely by 9 V and 6 V batteries, located inside the same box. The box has two BNC coaxial outputs for the dc lines and one triaxial output that carries the ac signal. The schematic of the electrical circuit in the box is shown in figure 3.3.

Due to the non-linear I(V) characteristics of a tunnel junction, we have to choose carefully the dc biasing scheme for the device. If the load line of our biasing circuit intersects the I(V) characteristic of the device more than once, the biasing can be unstable and introduce noise in our measurements. When the critical current is not suppressed, we would need a load line stiffer than 50Ω to be able to voltage bias at 100 μV without intersecting the critical current branch, on the order of 2 μA for our devices. To avoid this problem, we start the experiment by current biasing our device, switching to voltage bias once the critical current is suppressed below 50 nA.

After cooldown we first current-bias the junction through a 2 kΩ resistor. The critical current of a tunnel junction has a periodic behavior with the applied parallel magnetic field. Every time the flux Φ penetrating the junction is an integer of the flux quantum $\Phi_0 = 2.07 \times 10^{-15}\ Wb$, the zero-voltage current averages out to zero. We next adjust the magnetic field to correspond to one of the zeroes in the critical current. Usually the best suppression is achieved at the third zero, which requires a magnetic field of about 60 G. Once the critical current is suppressed by a factor of 10^{-2}, below 100 nA, we change to a more sensitive current scale by switching out the 2 kΩ resistor and connecting a 1 MΩ

resistor. We then suppress the critical current down to about 10 nA.

Given the good suppression of the critical current, we adjust the current-bias to zero and then switch to voltage-bias. We fine-tune the external parallel magnetic field for optimum critical current suppression. For voltage-biasing we use a loop in parallel with the input of a low-noise, large-bandwidth Amptek A250 amplifier, whose input needs to be kept at 3 V. The loop consists of two amplifiers: an OP97 that monitors the voltage across the device, and an OP77 voltage comparator. The OP77 compares the device voltage to a reference voltage and compensates the source-drain current of a FET connected at the input of the A250. This keeps the input voltage of the A250 at 3V. The junction is voltage-biased in the flattest region on the subgap I(V) curve, around 110 μV.

For both biasing schemes, the dc voltage is measured directly across the sample by an INA110 amplifier with a gain of 500. When current-biasing, the device dc current is inferred by measuring the voltage across the bias resistor. When voltage-biasing, the device dc current is inferred from the A250 output voltage. In both cases, the measured voltage is amplified with unity gain using an INA110 amplifier. Both dc signals go into ISO100 optical isolation amplifiers. These amplifiers prevent noise from coupling back to the device.

Outside the electronics box, the dc lines are sent through BNC cables outside of the shielding box. At the exit from the shielding box, the signals are filtered using custom-made T-filters [Wilson2002].

3.3.3 AC Electronics

The ac signal is amplified using the same A250 used for voltage-biasing, now in a trans-impedance configuration. The A250 is coupled to the device through a discrete input FET [Friedrich1997], making it a very good composite amplifier. The transistor that best matches our detector characteristics is the Toshiba 2SK146 FET. The composite amplifier draws current from the device on the feedback resistor, converting the input current into

an output voltage. The gain is set by the feedback resistor, which is 1 MΩ. The feedback resistor is anchored at the 1.5 K stage so that its Johnson current noise $S_I = \sqrt{4k_BT/R}$ is reduced to 9 fA/$\sqrt{Hz}$. The signal is further amplified by a factor of 10 with an INA110 amplifier.

The ac signal outside of the shielding box is carried by a short triaxial cable to a $12 \times 9 \times 6$ cm^3 box. There it is amplified by a factor of 10 using an INA110 amplifier. Amplifying the signal at this stage decreases the effect of pickup noise along the cables outside the shielding box. This box output feeds into a Princeton Applied Research (PAR) 113 amplifier, which is battery-powered during the experiment. The PAR is usually set to have a gain of 10 and to band-pass filter the signal in the $0.3 - 100$ kHz range. The lower frequency limit eliminates the 1/f noise. The higher frequency limit is on the order of the signal frequency and well within the A250 300 kHz bandwidth. This rejects higher frequency noise. The PAR output goes into the digital oscilloscope, where data are recorded.

3.3.4 Magnetic Field

In order to accurately measure the quasiparticle subgap current, we have to suppress the Cooper pair current. This is done by applying a magnetic field parallel to the junction plane. The magnetic field required for critical current suppression is produced by a pair of quasi-Helmholtz[3] superconducting coils made of NbTi wire. The field is adjusted by changing the current flowing through the coils, which is provided by a custom-built, battery-powered, high-current source located in a metal box inside the shielding box. The circuit board with the device is located in the center of the two coils, where the field is uniform and maximum.

[3]Helmholtz coils are a pair of circular coils on a common axis with equal currents flowing in the same sense. For a given coil radius, the separation needed to give the most uniform central field is equal to the radius of the coils. Our quasi-Helmholtz coils are separated by 7.75 cm, larger than the coils' 4.5 cm radius to allow a larger usable area on the cold finger.

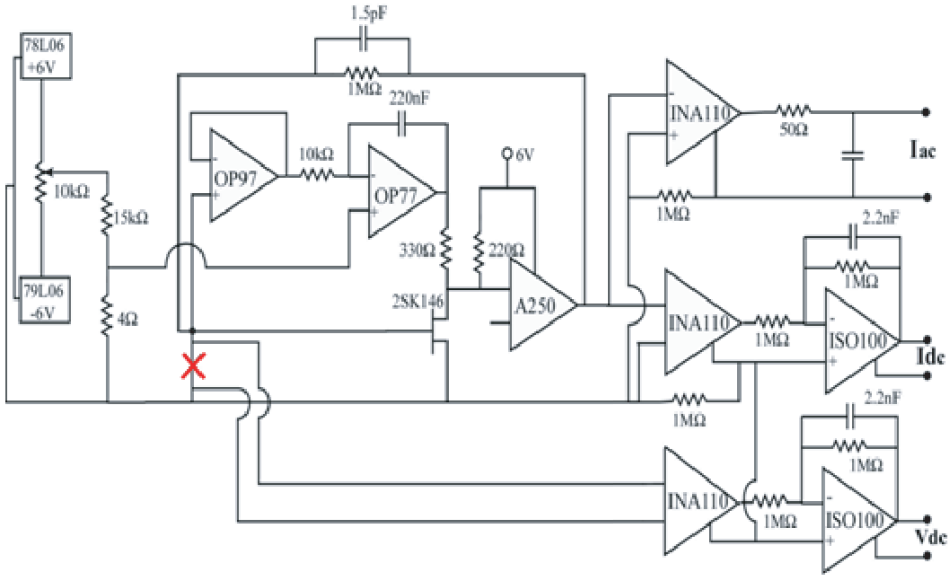

Figure 3.3: Active voltage biasing electronics, with the cross indicating our device.

3.4 Shielding

The experiments take place in a shielding box made by Lindgren RF-Enclosures, Inc.. The box is $1.6 \times 1.6 \times 1.6$ m^3, with 5 cm thick walls, providing electromagnetic shielding from 150 kHz to 10 GHz. Each 5 cm thick wall is made by 6 mm steel plates separated by plywood. The dewar is 64 cm tall and has a 36 cm outer diameter. A 3 mm thick mu-metal cylindrical shield, 50 cm tall and 47 cm in diameter, surrounds the lower half of the cryostat, where the cold finger is located. The mu-metal shield screens the static and low-frequency magnetic fields that would otherwise interfere with the device.

3.5 Optics

A detailed description of our optical setup can be found in [Wilson2002]. We test our devices with photons coming from either a Hg lamp which emits at different wavelengths, or from an ultraviolet (UV) pulsed VSL-337ND-S nitrogen laser, manufactured by Laser Science, Inc., whose output is at 337 nm. The light is guided through an optical fiber from either source to an optical bench. There it is filtered: we use color filters for single wavelength selection of the light coming from the lamp and neutral density filters for adjusting the intensity once we have monochromatic light. After the filters the light is collected into another optical fiber which feeds into the shielding box. From there another fiber is connected to a vacuum-tight feedthrough which goes into the dewar. Inside the dewar we have an Al-coated fiber, that wraps around the different cold stages. The fused silica fiber has a high OH content, the impurities absorbing the infrared radiation from room temperature and different cold stages. Thus we effectively filter the black-body radiation coming down the fiber from the cold stages. All fibers are terminated with SMA connectors except the fiber end that is aligned to the sample. We use multimode fibers that have a core diameter of 300 μm, a numerical aperture N.A.$= 0.22$, and operate at wavelengths between $250 - 800$ nm. The fiber is manually aligned to the devices. Usually it is located 1 mm away from the substrate. The light cone spreads over an area of 0.5 mm^2 on the substrate, four orders of magnitude larger than our device area. Using a singlemode fiber (with a much smaller core diameter) would decrease the area over which the photons are spread, but would make the light coupling into the fiber more difficult. We tried focusing the light onto the device, but the smallest spread area was still large, 0.03 μm^2.

The maximum internal pulse repetition rate of the laser is 30 Hz and the pulse width (FWHM) is less than 4 ns. The 'OptoSync' laser output provides an optically-derived TTL signal to allow synchronization of the external experiment with individual laser pulses. It has a very low temporal jitter relative to the laser pulse (< 1 ns), so we use it as a trigger

signal in our data acquisition system. The laser wavelength of 337 nm corresponds to an energy of 3.68 eV.

3.6 Data Acquisition

We use a 20 MHz digital oscilloscope, Nicolet Integra 40, for recording the pulses and noise traces. When the laser is used to test our devices, we use the TTL laser output signal 'OptoSync' as a trigger signal for recording the pulses. When the Hg lamp is our light source, the trigger level is set manually. Different data sets are acquired for different trigger levels. The levels are set around the value for which a significant change in the pulse detection rate is noticed.

Each pulse is digitized into 2000 points, with the first 500 points being the pre-trigger signal. Every 100 pulses the oscilloscope sends the data via a GPIB cable to the computer. A set of data is called a 'run' and it usually contains 4000 pulses. More pulses would provide better statistics, but the acquisition time for 4000 pulses is 20 minutes. The experimental time of 6 hours at the base temperature sets a hard limit on the time we have to allocate for exploring the large parameter space (such as different voltage biases and different light intensities) of our different device generations. Taking relevant data for at least a single-tunnel and a diffusion-engineered device during one cool down was paramount for extracting information that would determine our next generation designs. For noise measurements, we acquire long noise traces that are sent to the computer, where they are fast Fourier transformed. Typically 100 resulting noise spectra are averaged and the averaged spectrum is saved. The data are analyzed using existing and user-created procedures in IgorPro, a scientific graphing and data analysis software developed by WaveMetrics. We use the average pulse shape to optimally filter the pulses (the power spectrum of the noise is approximately constant in our measurement bandwidth). We obtain the charge by digitally integrating the current pulses.

Chapter 4

Fabrication

4.1 Overview

Our devices are fabricated using several steps of lithography. The chronological order of the steps involved is:

- Wafer oxidation
- Ta deposition on the whole wafer
- Resist spin and pattern - Ta ion-milling of individual chips
- Resist spin and pattern - Au deposition
- Resist spin and pattern - Al deposition

In this section I will explain the process of Si wafer oxidation, present the general principle of e-beam patterning, and introduce the microfabrication machines used. In the following sections, each fabrication step will be discussed individually in detail.

As device carriers we use 300 μm thick, 2" in diameter oxidized silicon wafers. Oxidation of Si refers to the process of growing a layer of silicon dioxide on the wafer surface. The silicon dioxide layer acts as an insulator between the different metallic structures to be fabricated and the substrate. The wafers are placed in a furnace for 60 minutes at a temperature of 1000° C. We use wet oxidation, which involves having a stream of water

vapors flowing across the wafers while in the furnace. We measure an oxide thickness of 225 nm using an interferometer.

The lithography is done with the field-emission high-resolution scanning electron microscope(SEM) FEI XL30 Sirion which has been converted into an electron beam (e-beam) writing system. We pattern the resist with an e-beam accelerated by 30 kV and having the sample at a working distance of 10 mm from the e-beam gun. For viewing the samples we use a 10 keV e-beam at a working distance of 5 mm. Using e-beam is necessary for gaining access to all sub-micron features, providing also a dynamic platform for design changes.

In transferring the desired patterns onto the oxidized wafer we use chemical substances sensitive to electrons, known as e-beam resists. For each metal layer step, we spin resist on a spinner located in a class 1000 cleanroom. The resist thickness is set by the resist type, the speed of the spinner vacuum chuck (usually several thousand rpm) and the spinning time (usually 60 seconds); for a thinner resist layer, we want a lower-viscosity resist spun fast and for a long time. After spin coating the wafer, we write our pattern with the e-beam into the resist. There are two types of e-beam resists: positive and negative. For positive resists, the resist is exposed with a beam of electrons wherever we want it to be removed. In these resists, exposure to the e-beam changes the chemical structure of the resist so that it becomes more soluble in the developer. The exposed resist is then washed away by the developer solution, leaving windows of the bare underlying material. Negative resists behave the opposite way, the developing solution removing only the unexposed areas. For all our processes, we use positive resists. The sample is developed for 48 seconds in a mixture of 1:3 methyl isobutyl ketone (MIBK) and isopropanol (IPA). The MIBK is the active solvent, while the IPA dilutes the MIBK, thus controlling the developing speed. The developing process is stopped by immersing the sample for 10 seconds in IPA. Nitrogen gas is used for blow-drying the sample.

For each patterning step we use different resist types and different process parameters. We use PMMA (polymethyl methacrylate) positive resist in anisole and MMA-MAA (copolymer) resist in ethyl lactate from MicroChem Corp. All the PMMA resist types used in our processes have a $950,000$ molecular weight and come in different concentrations in the anisole solvent. For example, 950PMMA A6 has 6% PMMA in anisole solvent. The copolymer is a mixture of PMMA and methacrylic acid in ethyl lactate solvent. MMA(8.5)MAA EL13 has 13% PMMA with 8.5% methacrylic acid in ethyl lactate. The copolymer offers a higher sensitivity to e-beam than PMMA, with a tradeoff in contrast. It is used as a bottom layer in bi-layers with PMMA, to produce undercut profiles.

The metal layers are deposited in the high-vacuum (HV) Lesker Sputtering System and in the Plassys electron beam evaporator system. The techniques used are dc-sputtering and thermal evaporation in the Lesker, and electron-beam evaporation in the Plassys. The Lesker system has a 3 cm Kaufman argon ion gun used for milling Ta and for ion-beam cleaning the samples before metal depositions. The Plassys system has an Anatech ion gun used for cleaning the samples before metal deposition steps.

After metal deposition on a patterned substrate, the resist with metal on top is removed using the lift-off technique. The sample is soaked in 75° C acetone for at least 20 minutes, followed by 1 minute of ultrasonic agitation. The metal on top of the resist lifts off as the resists dissolves in the acetone. The sample is rinsed with methanol before the acetone evaporates. The methanol is blow-dried with dry nitrogen gas.

For all the measured samples the Ta has been deposited in the Lesker system and the Au in the Plassys. The Al on Chip1 was deposited in the Lesker via thermal evaporation, while for Chip2 and Chip3 were deposited in the Plassys e-beam evaporator. In the next sections I will describe in chronological order the device fabrication steps on the oxidized wafer.

4.2 Ta Deposition

We start by dc-sputtering tantalum in a Lesker thermal evaporator/dc-sputtering system. We let the wafer bake at 350° C for 12 hours in the vacuum chamber until the pressure goes down to 2×10^{-8} Torr. We then clean it with an ion-beam for 2 minutes just before the deposition. The Ta is heated up to at 750° C and then sputtered at a rate of 10 nm/s over the whole wafer. We let the wafer cool for 3 hours without breaking vacuum. All the measured samples were fabricated using the same 70 nm Ta wafer.

4.3 Ta Ion-Milling

We spin a 2500 nm double layer of MMA(8.5)MAA EL15/950PMMA A8 (positive resists) on the whole wafer covered with sputtered Ta. The parameters for the resist process are listed in table 4.1. We then cut the wafer into several chips using a diamond tip scriber and continue the next steps on each individual chip. The writing 'unit cell' consists of 4 devices that will share the same Ta alignment marks. Each set of 4 devices covers a chip area of about 4×6 mm^2. The e-beam patterning is done such that there is no resist where we want the Ta to be removed.

We use the Lesker ion-gun to ion-mill the Ta which is not covered by resist. The ion-beam current is 4.7 mA and the beam voltage 500 V. Etching away 70 nm Ta takes about 9 minutes. The thick double resist layer is used to protect the Ta under it during the milling process. The left-over resist is removed in an ultra-sound bath while soaking in hot acetone. The only features on the chip are now one Ta plug per device and a set of 4 alignment marks for each set of 4 devices.

4.4 Au Deposition

Gold electrodes form the second layer. We spin 950 PMMA A6 at 2000 rpm for 1 min and bake it at 170° C for 30 min. The resist thickness is 600 nm. We pattern it such that

Resist	MMA(8.5)MAA EL15	950 PMMA A8
Spinning speed [rpm]	1500	3500
Spinning time [min]	1	1
Baking temperature [°C]	170	170
Baking Time [min]	1	25
Cooling time [min]	1	1
Resist thickness [nm]	1750	750

Table 4.1: Resist process parameters for Ta

the regions we want Au deposited on are not covered by resist. We use the Ta alignment marks to align our e-beam writing to the previous existing structures.

The parameters used for the Au deposition are summarized in Table 4.2. We first clean the sample with an ion beam for 2 minutes. A thin 3 nm layer of Ti is first deposited at a 0.2 nm/s rate. It is used to enhance the Au adhesion to the SiO_2 surface. The 100 nm thick Au layer is deposited at a 0.5 nm/s rate. This is a thickness for which the wire-bonding to the Au pads quality is consistently good.

Pressure [Torr] Before	Chip1 and Chip2 [Chamber/Load Lock]	Chip3 [Chamber/Load Lock]
Ion Beam Cleaning	1.7×10^{-7} / 1.7×10^{-6}	1.0×10^{-7} / 6.5×10^{-7}
Ti Deposition	1.8×10^{-7} / 1.1×10^{-6}	7.6×10^{-8} / 4.9×10^{-7}
Au Deposition	3.1×10^{-8} / 3.3×10^{-7}	8.0×10^{-9} / 2.0×10^{-7}

Table 4.2: Parameters for Au deposition in the Plassys.

4.5 Junction Fabrication

The tunnel junctions are fabricated using the Dolan-bridge technique [Dolan1977]. A double-layer of MMA/PMMA resist is spun on the chip, with the parameters found in Table 4.3.

Two openings which later will become the junction electrodes are patterned 1 μm apart in the resist. Due to the faster solubility of the exposed copolymer than that of the exposed PMMA in the developer, we create an undercut in the lower resist layer. The space be-

Resist	MMA(8.5)MAA EL15	950 PMMA A6
Spinning speed [rpm]	2000	2000
Spinning time [min]	1	1
Baking temperature [° C]	170	170
Baking Time [min]	1	30
Cooling time [min]	1	1
Resist thickness [nm]	1450	550

Table 4.3: Resist process parameters for Al junctions.

tween openings being comparable to the undercut size, a hanging resist bridge (made of the second resist layer) is created after the developing process. Figure 4.2 sketches this technique.

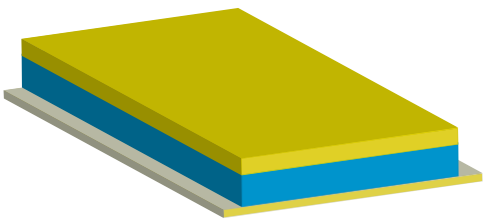

(a) Start with a double layer of resist

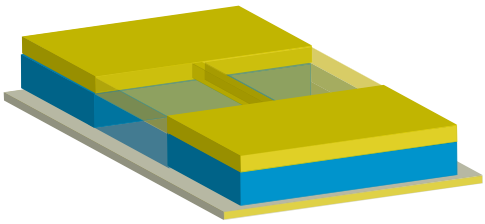

(b) Expose 2 rectangles which are apart a distance on the order of the undercut.

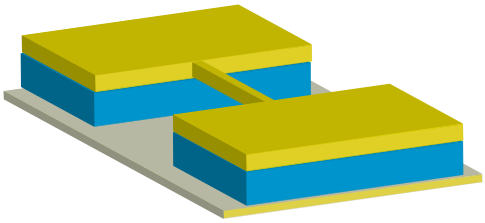

(c) Develop the resist and obtain a resist bridge from the second resist layer.

Figure 4.1: The Dolan-bridge patterning technique [not to scale].

Before the Al deposition, the sample is ion-beam cleaned for 2 minutes. The first Al layer has an effective thickness of 50 nm and is deposited at an angle of 40° from the normal to the sample. We let the sample cool down for 2 minutes and then oxidize it to form the junction. By varying the amount of time and the dry O_2 pressure during oxidation we can change the junction transparency, i.e. the super-current density. We then pump out the O_2 and deposit the second layer of 70 nm Al perpendicular to the sample.

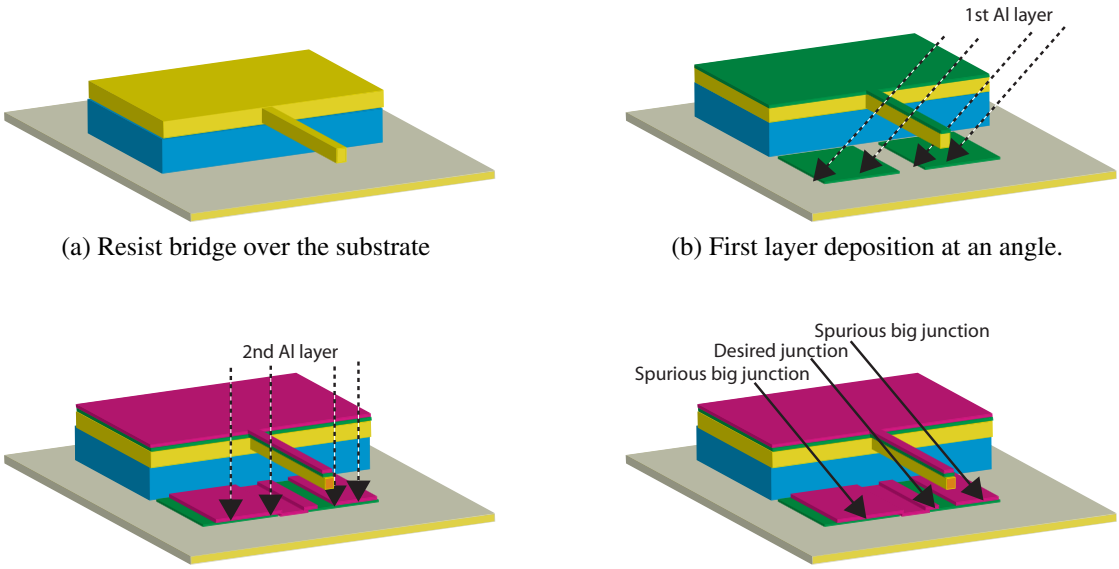

(a) Resist bridge over the substrate

(b) First layer deposition at an angle.

(c) Second layer deposition perpendicular to the sample.

(d) Resist ready for lift-off

Figure 4.2: Cross-sectional view of the Dolan-bridge double-angle evaporation technique [not to scale].

The Al on Chip1 is deposited in the Lesker. The system is pumped down to 3×10^{-8} Torr before the ion-beam cleaning. The junction is formed by oxidation at 1 Torr for 20 minutes. We then pump out the oxygen, reaching a 2×10^{-6} Torr pressure and deposit the second Al layer. The Al deposition rate was for both electrodes 0.3 nm/s.

The Al on Chip2 and Chip3 is deposited in the Plassys. We begin by evaporating titanium at a rate of 0.1 nm/s for 50 seconds with the shutter covering our sample. The Ti deposition helps to lower the pressure in the vacuum chamber, without being deposited on our samples. The aluminum is deposited at a 1 nm/s rate for both electrodes. The oxidation is done in a mixture of Ar/O_2, with 15% partial pressure of O_2 in Ar. Table 4.4 has the process parameters.

The Al in the three samples has been deposited in the presence of different oxygen levels. This affects the purity of the Al, changing its superconducting energy gap and its diffusion constant. The oxidation process parameters, the oxygen flow during the deposition and the transparency of the junctions for the three samples are summarized in table 4.5.

Pressure [Torr] Before	Chip2 [Chamber/Load Lock]	Chip3 [Chamber/Load Lock]
Ion Beam Cleaning	3.3×10^{-8} / 5.4×10^{-7}	9.6×10^{-8} / 2.8×10^{-7}
Ti flow	1.1×10^{-7} / 5.0×10^{-7}	1.0×10^{-7} / 2.8×10^{-7}
1st Al Deposition	2.0×10^{-8} / 1.5×10^{-7}	6.7×10^{-9} / 1.2×10^{-8}
Oxidation	6.2×10^{-8} / 7.0×10^{-7}	6.2×10^{-8} / 1.9×10^{-7}
2nd Al Deposition	1.9×10^{-7} / 5.0×10^{-7}	1.6×10^{-7} / 8.2×10^{-7}

Table 4.4: Parameters for Al deposition for junctions fabricated in the Plassys

Sample	System	O_2 flow	Oxidation time [min]	Oxidation pressure [Torr]	$j_C[A/cm^2]$
Chip1	Lesker	0	20	1	39
Chip2	Plassys	0.4 sccm	10	3	78
Chip3	Plassys	0.5 sccm	18	1	148

Table 4.5: Parameters for Al film deposition and junction oxidation.

After the sample is taken out of the evaporator, the resist is removed by the usual ultrasound bathing in hot acetone. During this step the acetone temperature is only 65° C to prevent junction degradation that would occur at higher temperatures.

4.6 Device Layout

4.6.1 Design Files

The devices are designed using the DesignCAD software. The different layer designs for a particular device can be present in the same *.CAD file.

The Run File Editor is used to record the exposure conditions for the different drawing elements of a CAD file. The *.run files embed the DesignCAD files into the Nabity Nanometer Pattern Generation System (NPGS) program that controls the SEM. One can easily change doses in a *.run file without changing the pattern design.

The correct dose for a pattern is not determined only by the resist sensitivity. The dose we set in our *.run files only describes the primary electrons, coming down the microscope column. The secondary electrons created by the primary beam also contribute to the effective dose. A higher beam energy will cause deeper penetration into the sub-

strate and consequently fewer backscattered electrons will reach the surface. A larger dose will be required and finer lines can be obtained when compared to lower energy beams. We write with the highest beam energy of 30 keV and the area doses used are in the $300 - 350\ \mu\text{C/cm}^2$ range.

The magnitude of the beam current affects the spot size. In every electron microscope, the size of the beam hitting the sample, i.e. the spot size, will be the smallest at the highest possible accelerating voltage and the lowest beam current. These are the conditions for writing the finest structures. When writing larger structures, it is desirable to use a high beam current (larger spot size) so that the writing time can be minimized. The downside is being limited to a much larger minimum feature size.

When the beam current or the magnification is changed, there can be unwanted offsets between different layers of a single pattern or between different sets of alignment windows. We check beforehand for the offset between different magnifications and we correct for it in our run file. The shift on one axis between the small writing field of $187 \times 187\ \mu m^2$ at a magnification of 1000 in spot 1 and the larger field of $1870 \times 1870\ \mu m^2$ at a magnification of 100 in spot 7 can be as large as $7\ \mu m$ on each axis.

We can align different layers by using the align feature in the NPGS software. Patterns may be aligned to existing alignment marks without exposing the writing area, by using an alignment program. Our alignment file has 2 sets of alignment windows: a large, coarse one, followed by a smaller, fine one. Each set has 4 windows defined within the field of view of the microscope. Within each window there is an overlay pattern that has to be aligned to a real alignment mark on the sample. The overlaying patterns and the sample area within the windows are simultaneously displayed on the PC screen. Each window can be individually manually aligned. The program then calculates a general transformation matrix that corrects for the sample rotation and offset. The matrix is used by the pattern generator when writing patterns to give accurate registration between lithography levels.

The design for the Ta layer is presented in Figure 4.3. The resist in the written regions

will be developed in an IPA/MIBK solution. We want to expose the areas that we want the Ta to be removed from and not to expose the areas we want it to stay. In the DesignCAD layout from Figure 4.3, the different colors represent patterns written with different spot sizes. Due to shifting offsets, we have to give a margin of error in the alignment of structures written with different magnifications in different spot sizes. We do this by creating a small overlap between these structures.

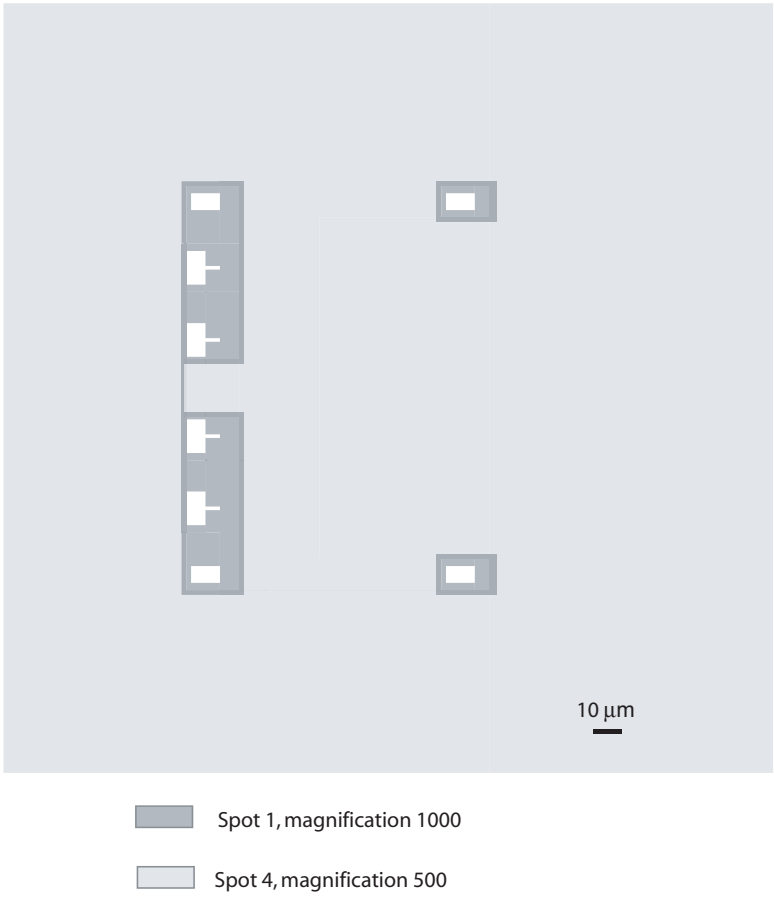

Figure 4.3: Layout of resist pattern for the Ta layer.

The layout of the Au and Al layers is shown in Figure 4.4, without displaying the Ta plugs and alignment marks.

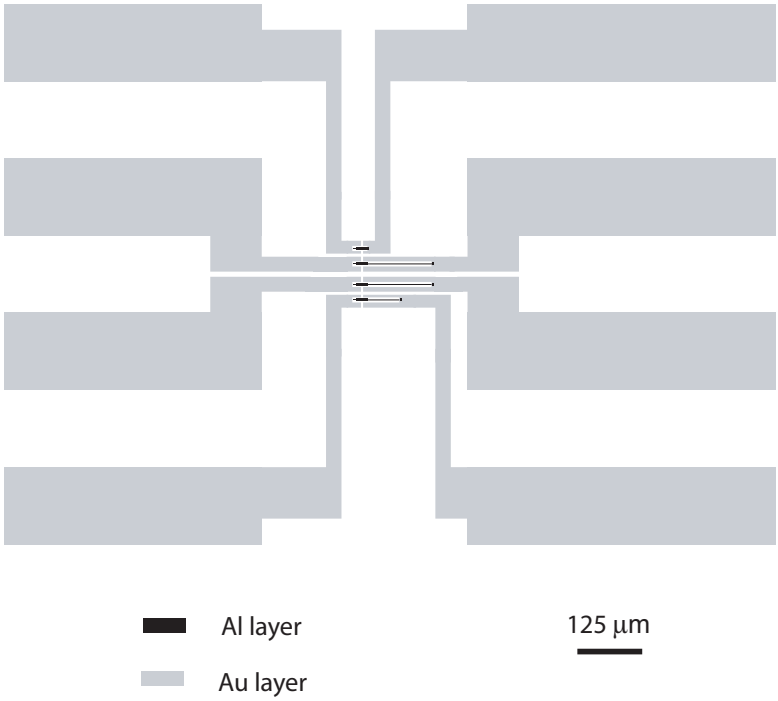

Figure 4.4: Layout of resist pattern for the Au and Al layers.

4.6.2 Device Imaging

We image our devices using an optical microscope that has a maximum magnification of 1500. To see details of features smaller than 1 μm we use SEM imaging.

The optical micrograph of the central part of Chip2 is shown in Figure 4.5 at a magnification of 500. Zooming in with the SEM, we see in Figure 4.6 a single-tunnel and a diffusion-engineered junction (with the out-diffusion wire partially truncated) from the same chip.

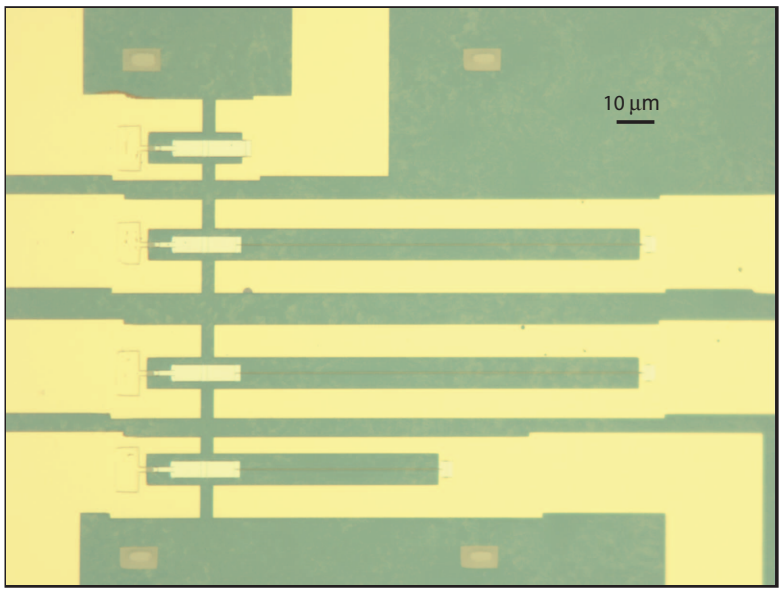

Figure 4.5: Optical micrograph of Chip2 excluding part of the leads at a magnification of 500.

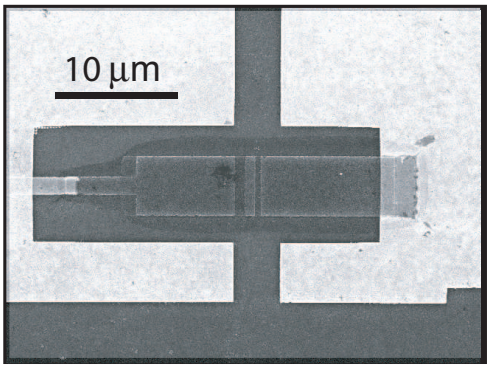

(a) Single-tunnel Device

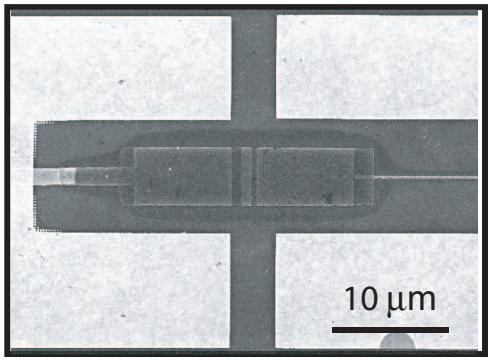

(b) Diffusion-Engineered Device

Figure 4.6: SEM pictures of devices.

Chapter 5

Experimental Results

This chapter presents experimental results from single-tunnel and diffusion-engineered devices. The charge signal created by an absorbed photon in a diffusion-engineered device is increased (via backtunnelling), compared to the charge signal created in a single-tunnelling device by the same photon. Thus, using diffusion-engineering, single-photon resolution is improved for photons in the UV and visible spectrum.

First I will describe how we developed the design for single UV-photon sensitive devices, followed by data from an early design device tested at 50 mK. The expected response of our devices to laser pulses will then be explained in detail. Before the presentation of single UV photon measurements, I will explain how we control the Al diffusion constant, which allows us to control the charge increase in the diffusion-engineered devices (as explained in the theory chapter). I will then summarize the results and discuss the improvement in the energy resolution attained with the diffusion-engineered devices.

5.1 Research Path

The implementation of the new diffusion-engineering approach for backtunnelling devices benefitted from the availability of a reliable and high-resolution e-beam writer. The STJs for previous research [Wilson2002] were fabricated using an optical lithography tri-layer junction process, followed by wet etch patterning. The device geometries were set by the pre-made optical masks, lacking the design dynamism associated with e-beam writing,

where one can adjust the device design with every patterning. In addition, optical lithography and wet etching limited the minimum size of the junction to about 7 μm. As explained at the end of the theory chapter, smaller area junctions have a smaller quiescent current I_{dc}, and therefore a smaller current noise i_n. Consequently, we used completely different fabrication techniques then before, the most important ones being: e-beam lithography instead of photolithography, and Dolan bridge double-angle deposition instead of tri-layer tunnel junction technique. All junctions were designed to be $1 \times 5\ \mu m^2$. The different device generations are schematically illustrated in Figure 5.1 and optical micrographs of real devices are shown in Figure 5.2.

We started the diffusion-engineering project by researching the reliability in the fabrication parameter space (described in the fabrication chapter by the junction fabrication parameters) of e-beam Al junctions. We wanted to have a solid, reproducible junction fabrication process for double-angle evaporation using e-beam lithography. We improved our process by testing the devices cold, and analyzing their I(V) characteristics. In these all-Al devices a good energy resolution was not expected.

Later, an absorber was defined by depositing Nb on top of one of the Al electrodes. Nb had been found to have a high density of quasiparticle trapping centers, not being ideal as a photon absorber. Our choice was forced by the fact that Ta sputtering gun in the Lesker deposition system was broken at the time. None of these devices provided good enough energy resolution for single UV photon detection.

5.1.1 Ta-absorber Devices

Once the Ta gun was fixed, we deposited Ta on a new wafer and started incorporating it into our detectors' design. We started with devices whose geometry is depicted in Figure 5.1a having:

1. Ta absorber
2. Al junction overlapping Ta absorber

3. Ta absorber connected through a narrow Ta wire to the Al left pad

There was no photon-number resolution from the two tested single-tunnelling devices. We thought the responsivity was too low due to quasiparticles escaping down the narrow Ta wire and being trapped into the Al left pad.

Next generation (E04_Diff_Ta6) of devices, shown in Figure 5.2a, included:

1. Ta absorber

2. Al junction overlapping Ta absorber

3. Nb contact from the Ta absorber to the Al left pad.

This design didn't provide a better response of our junctions to UV photons. We realized that the small Al trap volume necessary for a fast tunnelling time were not allowing the quasiparticles to be trapped efficiently from the Ta absorber. Not having enough time to relax down to the Al energy gap in the trap, the quasiparticles would diffuse back into the Ta, and not tunnel across the junction. In the absorber, the quasiparticles would eventually recombine and be lost.

Making the trap volume bigger to facilitate faster trapping would have increased the tunnel time unless we made the junction larger, which would give a lower normal state resistance. Having a larger junction would thus give a larger subgap current, and therefore an associated larger current noise. One solution was to have the trap itself be the absorber.

5.1.2 Al-absorber Devices

The next design, shown schematically in Figure 5.1b had:

1. Al absorber (the two junction electrodes)

2. Ta 'plug' connected to Al wiring on the left and through a narrow Al wire to the left electrode

After not having discriminated single photons, we decided to mask the whole device except for the electrodes. We deposited a 200 nm SiO insulator and 100 nm Au on top, as a reflector. The device (Aljct_1_R), with the Au mask on top, is shown in Figure 5.2b. We

were not able to bias the device due to electromagnetic cavity resonances we had created by adding the mask. These resonances appeared as structure in the subgap I(V) curve.

Next we decided to have the wiring pads made out of Au, to better reflect photons from areas outside the absorber. From the previous generation we also had proof of fast device ageing (device gradually increasing its resistance within a week, until becoming open). We thought this was due to a slowly degrading small-area interface. Since the ageing process was common to all geometries, we reasoned the culprit must have been the $1 \times 3\ \mu m^2$ interface between the Ta plug and the Au pads. The geometry for these devices is shown in Figure 5.1c, and Figure 5.2c shows a device picture.Thus we increased this area by a factor of 15, as shown schematically in Figure 5.1d and in an optical micrograph of a device in Figure 5.2d. This is the design we used for all the devices that had photon-number resolution.

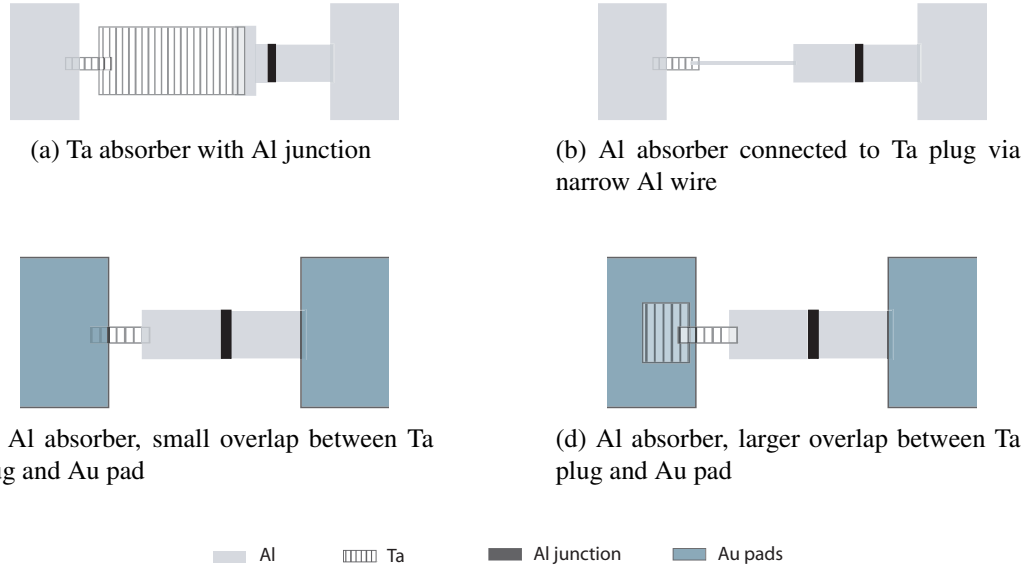

(a) Ta absorber with Al junction

(b) Al absorber connected to Ta plug via narrow Al wire

(c) Al absorber, small overlap between Ta plug and Au pad

(d) Al absorber, larger overlap between Ta plug and Au pad

Figure 5.1: Sketches of different device generation design [not to scale]. The scale is set by all the junctions being $1 \times 5\ \mu m^2$.

5.2 Dilution Refrigerator Measurements

Sample $B-C2-TF$ from chip $OPS-E03-STJ4B$ is an aluminum-only device, with a normal resistance $R_n = 93\ \Omega$ and an energy gap $\Delta = 170\ \mu eV$ at $T = 50$ mK. The two

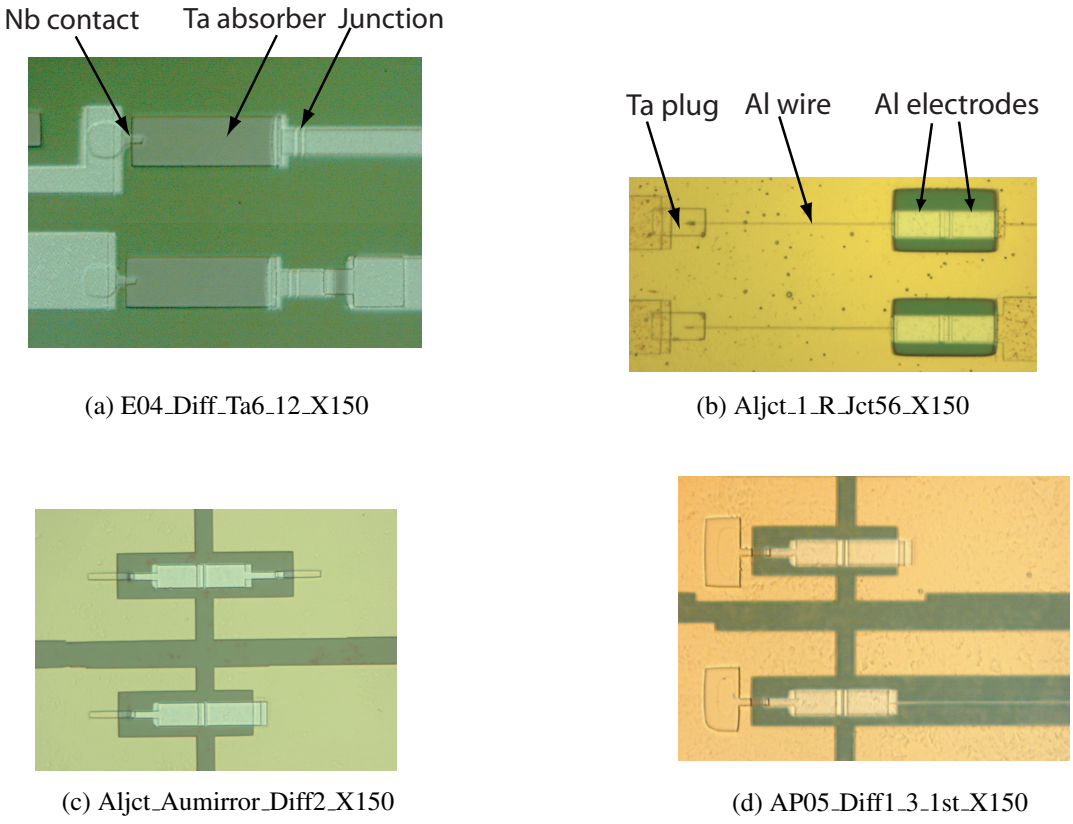

(a) E04_Diff_Ta6_12_X150

(b) Aljct_1_R_Jct56_X150

(c) Aljct_Aumirror_Diff2_X150

(d) AP05_Diff1_3_1st_X150

Figure 5.2: Consecutive device geometry generations.

$5 \times 26\ \mu m^2$ electrodes are terminated on one side by a $0.4 \times 360\ \mu m^2$ narrow lead, and on the other by a $5 \times 370\ \mu m^2$ wider lead, as seen in Figure 5.3. It was the only device measured in our Oxford dilution refrigerator, at a base temperature of 46 mK.

Only 2-wire dc measurements were performed. We investigated the variation of the gap and of the critical current with an externally applied magnetic field parallel to the junction barrier, and that of the subgap current with temperature.

A magnetic field parallel to the junction area should suppress the energy gap of a superconductor. According to the Ginzburg-Landau theory of superconductivity, the gap should decrease with magnetic field as in equation 5.1, disappearing when the field reaches a critical value H_C:

$$\frac{\Delta(H)}{\Delta(0)} = \sqrt{1 - \left(\frac{H}{H_C}\right)^2} \tag{5.1}$$

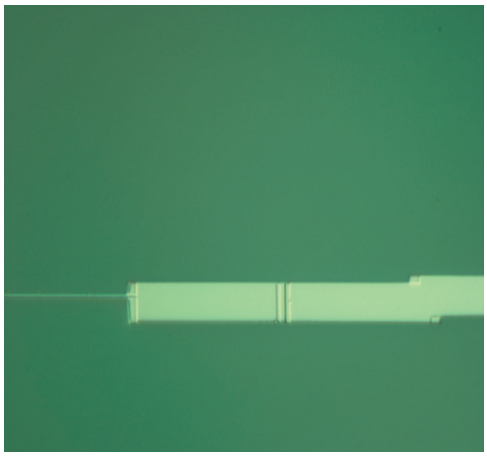

Figure 5.3: Optical micrograph of sample $B-C2-TF$.

The measured the I(V) curves for different magnetic field values are shown in Figure 5.4.

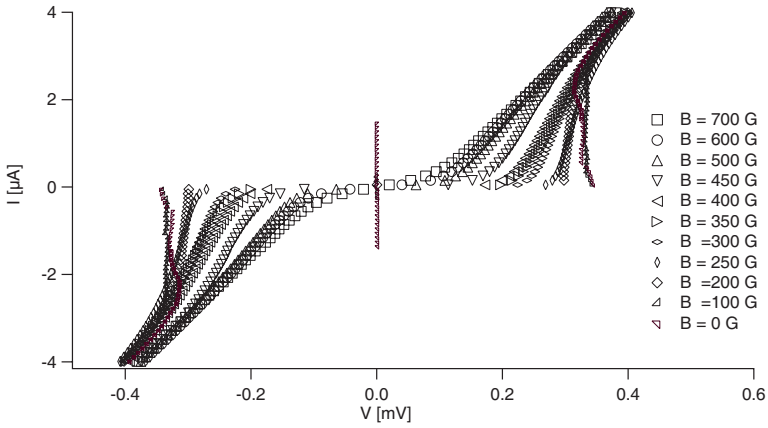

Figure 5.4: Measured I(V) curve at different magnetic field values, at 46 mK.

The fit of the data to equation 5.1 is shown in Figure 5.1. We obtain a critical field $H_C = 510$ G.

The first zero in the critical current occurred at a field $B = 62$ G, but the best suppression was achieved at the third zero $B = 164$ G, as seen in Figure 5.6.

The subgap current was recorded at different temperatures, as seen in Figure 5.7. This was the first time the junctions fabricated in our group were measured at temperatures below 215 mK. The critical current was nearly suppressed at the base temperature of 46 mK

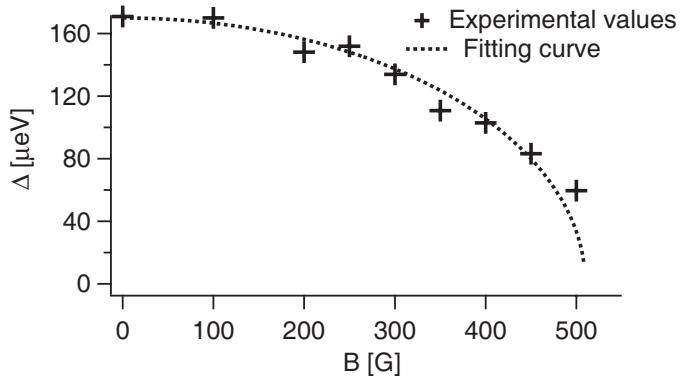

Figure 5.5: The energy gap measured as a function of magnetic field at 46 mK.

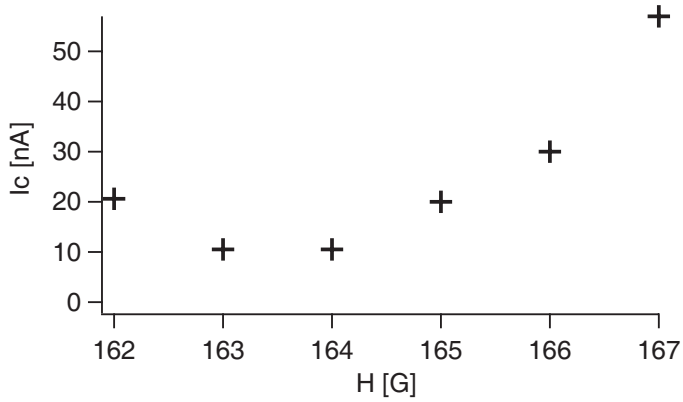

Figure 5.6: Measured critical current versus applied parallel magnetic field at 46 mK.

with a parallel field of 164 G. The temperature was increased to 350 mK, with the junction biased at 110 μV. The measured and theoretical curves of the subgap current versus temperature are showed in Figure 5.8. Below 230 mK the experimental values start to diverge from the ones predicted by the BCS theory. The current saturates around 160 mK at a constant value of 60 pA, called the sub-gap leakage current. A similar behavior was seen in 23 μm^2 Al junctions having half the critical current density of our junctions [Subgap2001]. Among the possible explanations for the sub-gap leakage seen in our devices are imperfect super-current suppression, extra noise limiting the sensitivity of our measurement and pin-holes in the junction oxide.

Similar experiments have been done in Prof. R. Schoelkopf research group by J. Teufel [Teufel2007]. They measured an Al junction with a normal resistance of 92 $k\Omega$

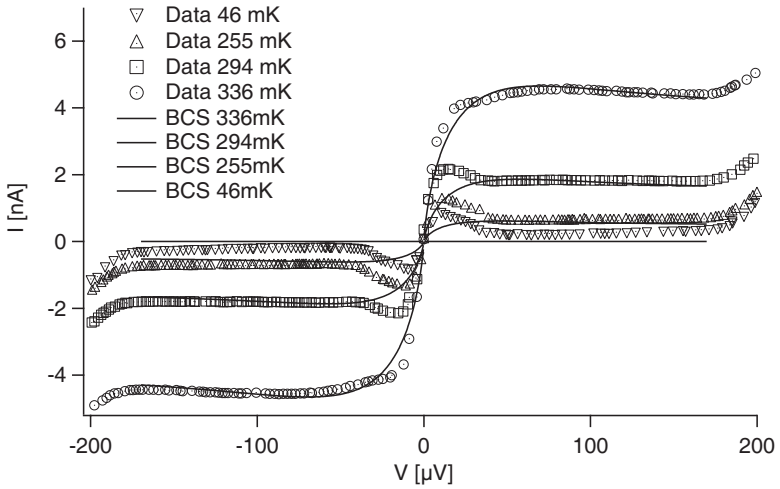

Figure 5.7: Measured subgap current and the associated theoretical BCS curves for different temperatures.

and a gap of 225 μeV. The junction followed the BCS predictions down to about 170 mK [Prober2006].

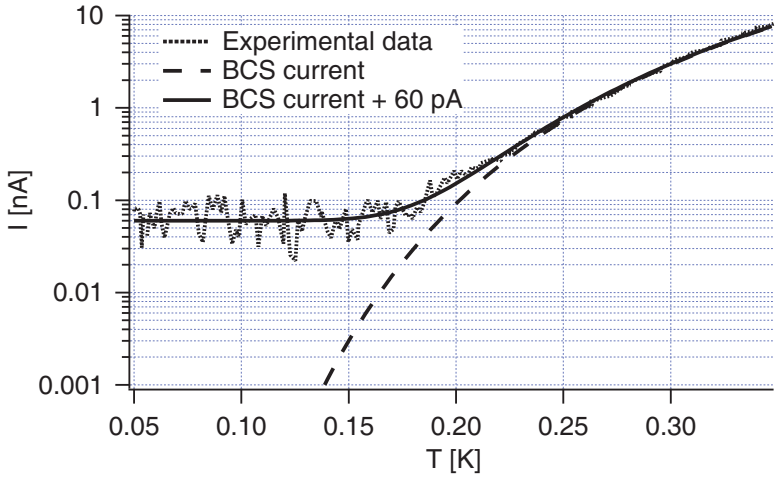

Figure 5.8: Measured subgap current versus temperature. The junction has a normal resistance $R_n = 93\ \Omega$ and the electrodes are terminated by a narrow lead on one side and by a wider lead on the other. The fit includes an extra 60 pA of current added to the theoretical BCS curve, an empirical procedure.

5.3 Device Response to UV Photons

5.3.1 Ideal Poisson Distribution of Photons

The number of photons emitted by a laser obeys Poisson statistics and is not constant in every burst. The Poisson distribution expresses the probability of a number of events occurring in a fixed period of time (in our case number of photons per pulse), if the average rate with which they occur is known and if they are independent of each other. The probability of having exactly n events happening given that on average there are $\overline{N}$ events is:

$$P(n) = e^{-\overline{N}} \frac{\overline{N}^n}{n!} \tag{5.2}$$

Figure 5.9 shows the histogram of the number of laser pulses out of a total of 4000 having a different number of photons, for a Poissson distribution characterized by an average number of photons $\bar{N} = 0.5$. The number of photons coming out of the laser is attenuated by filters and imperfect optical connections down to the absorber. The attenuation effectively decreases the average number of photons that reach the absorber.

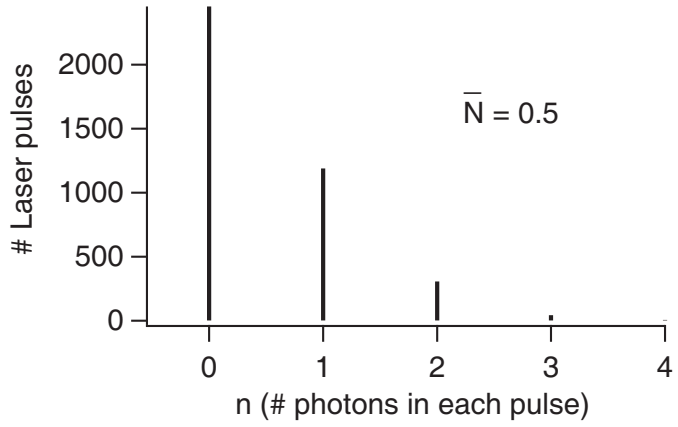

Figure 5.9: Ideal Poisson distribution of photons with an average number of photons of 0.5.

The time width of a burst is much narrower than the smallest relevant time scales of our experiment. This means that if, for example, 2 photons of energy E are absorbed in

one pulse, the device will respond as if it had absorbed one photon of double the energy. Assume the distribution of the number of pulses as a function of the number of photons in each pulse that are absorbed in our devices is described by the average number $\bar{N} = 0.5$. Then the distribution of the number of pulses as a function of the charge in each pulse will be characterized by the same average number $\bar{N} = 0.5$. Thus the Poisson distribution is mapped from the optical to the charge domain. This gives us in principle the possibility of testing our devices at any energy multiple of 3.68 eV. This is not true unless we have a device whose absorber is the only photon-sensitive area. Increasing the number of photons that land on the absorber also increases the number of photons that land on the device's wiring and on the substrate, which covers a much larger area than the absorber. For each photon landing on the absorber, we have about 10^4 photons landing outside of it, as explained in the setup chapter. These photons absorbed outside create substrate phonons which couple to the detector and break an undetermined additional number of Cooper pairs, creating excess noise. Thus for every laser pulse for which zero photons are absorbed in our absorber, there is a non-zero number of photons landing close enough to the junction to give a strong phonon signal. We read out this signal as a spurious pulse with a finite charge, which we call the offset charge. Our devices lose their single-photon resolution at an average number of around 5 absorbed photons.

For every detected charge Q, the noise in our detection system adds an uncertainty ΔQ to it. The charge histogram of many pulses generated by the same number of photons will have a Gaussian distribution. The full width half maximum (FWHM) of this distribution determines the energy resolution of our measurement.

We exemplify the difference between the ideal Poisson distribution and our devices' response to it in Figure 5.10. Each charge response has an associated width to it due mainly to the noise in our system, amplifier noise and noise from photons absorbed outside the absorber. The zero peak (n = 0) is shifted by an offset charge which is also due to photons absorbed outside the absorber.

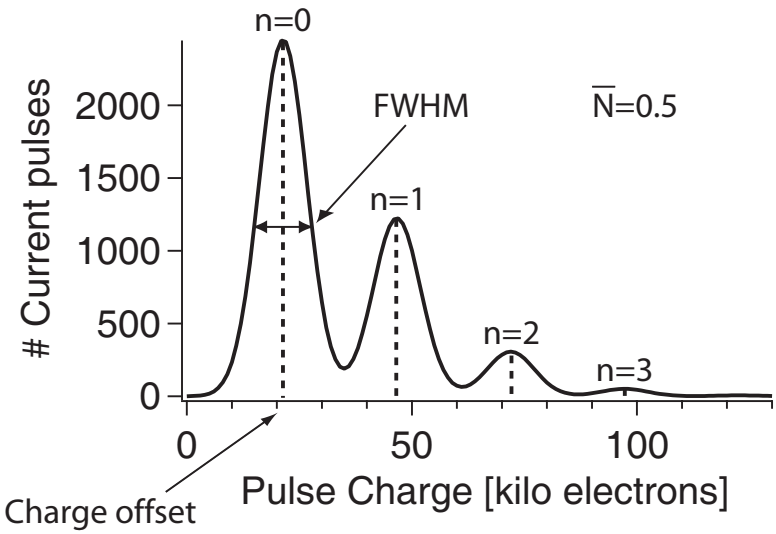

Figure 5.10: Non-ideal detection of an ideal Poisson distribution of photons with an average number of photons of 0.5.

The charge histogram obtained from each run is fitted to a distribution formed of multiple Gaussians evenly spaced in charge:

$$P(Q) = \sum_{n=0}^{\infty} \left(e^{-\overline{N}} \frac{\overline{N}^n}{n!} \right) \frac{1}{\sqrt{2\pi\sigma^2}} exp\left(-\frac{1}{2\sigma^2} (Q - (R \times nE_{photon} + Q_0)^2) \right) \tag{5.3}$$

There are several fit parameters in the distribution. The responsivity R measures how many charge excitations were read out per unit energy of the incoming photon; the average number of absorbed photons $\overline{N}$; the standard deviation of the charge σ, which is translated into an energy resolution via the responsivity; and the charge offset Q_0, which is the average charge of the pulses recorded when there was no photon absorbed in our devices, measured as the average charge of the peak $n = 0$ in the charge histogram.

5.3.2 Diffusion in Al

Having a material with a smaller diffusion constant lets us test devices with long outdiffusion times without increasing the number of squares in the outdiffusion lead. We can achieve a smaller diffusion constant by increasing the oxygen impurities in the Al. This is done by having a constant flow of oxygen in the deposition chamber during the Al evap-

oration. Table 5.1 presents results obtained by evaporating 50 nm of Al with different oxygen concentrations in a $0.15 \times 30\ \mu m^2$ trench. Assuming a rectangular cross-section, the conductivity σ of the wire is $\sigma = \frac{L}{Rwt}$, where L, w and t are the wire's length, width and thickness, respectively. R is the normal state resistance measured just before the superconducting transition. We use Einstein's relation, $\sigma = N_n(\varepsilon_F)e^2D$, to find the diffusion constant D. $N_n(\varepsilon_F)$ is the density of states per unit energy at the Fermi level in the metal[1]. The conductivity of the sample can also be expressed as the inverse of the resistivity ρ. For the first and last sample the transition temperature was not recorded.

Oxygen flow	Pressure during evaporation	ρ	D_n	T_C
[sccm]	$[T]\times 10^{-5}$	[$\mu\Omega$ cm]	[cm^2/s]	[K]
0.4	1.5	20	9.0	–
0.5	2	72	2.5	1.96
0.6	2.2	155	1.2	2.11
0.75	2.5	266	0.7	2.19
0.8	4.1	386	0.47	–

Table 5.1: Al film parameters as a function of the O_2 concentration during evaporation.

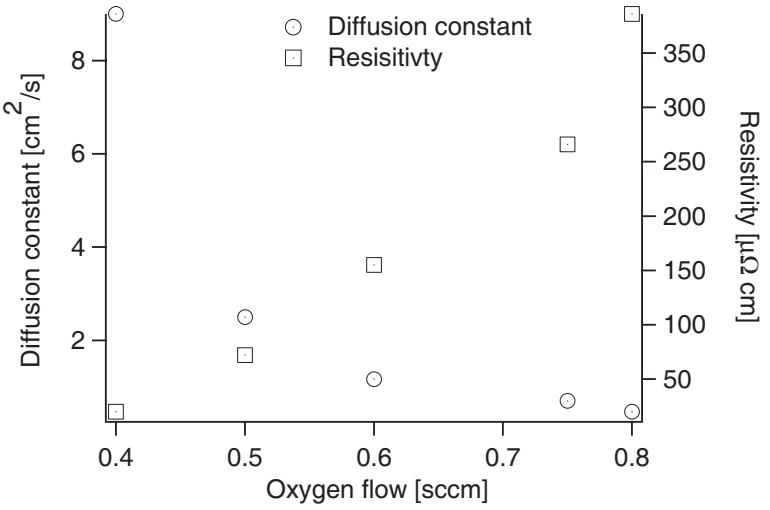

Figure 5.11: Diffusion constant D and resistivity ρ as a function of oxygen flow during Al deposition. Devices fabricated and measured by F. Pierre, C. Rigetti, and C. M. Wilson at Yale University.

[1]We are using here the density of states at the Fermi level as found in [Anthore2003], $N(\varepsilon_F) = 2.15 \times 10^{47}$ states/(Jm^3).

In the superconducting state, the quasiparticle diffusion constant is reduced compared to its normal state value. This is due to the quasiparticle dispersion relation exhibiting a minimum at the Fermi energy, where the density of states diverges. This approach of the quasiparticle group velocity to zero dictates a smaller superconducting diffusion constant, which for thermal equilibrium has been computed by [Narayanamurti1978] to be:

$$D_{qp} = D_n \sqrt{\frac{2k_B T}{\pi \Delta}} \tag{5.4}$$

5.3.3 Aluminum Devices with $\Delta = 170\ \mu eV$ (Chip1)

Our 'clean' Al devices had the Al electrodes deposited in high-vacuum, in the absence of oxygen. The parameters for these devices are shown in Appendix B. The junctions had an energy gap $\Delta = 170\ \mu eV$ and a normal state resistance $R_n = 133\ \Omega$. The types of devices tested were: single tunnel device (Chip1_st), 'short diffusion-engineered' device with a $0.25 \times 62\ \mu m^2$ outdiffusion lead (Chip1_sd), and 'long diffusion-engineered' device with a $0.25 \times 125\ \mu m^2$ outdiffusion lead (Chip1_ld).

The optical testing of the single tunnel device was done using a room temperature, 1 MΩ feedback resistor, which added extra Johnson current noise to the measurements. A 1 MΩ cold resistor was used for the feedback, but the electrical connections to it were unstable during that measurement. This in conjunction with temporary and unusual electrical interference from the laser significantly decreased the sensitivity of the device. The pulses from the laser photons had a characteristic decay time of $4.9\ \mu s$, and an estimated responsivity of 1200 electrons/eV.

The other two types of devices were measured with a cold feedback resistor and no electrical interference from the laser. Figure 5.12 shows the current vs. voltage characteristics of Chip1_sd and Chip1_ld after the critical current was optimally suppressed in each device. The deviation from the BCS shape for Chip1_sd is probably due to imperfect suppression of the critical current, which can be due to non-uniformities in the oxide barrier.

Chip1_ld shows a deviation from the BCS shape in the opposite direction. This can be an averaging effect of the voltage bias, if there is noise below 1 nA.

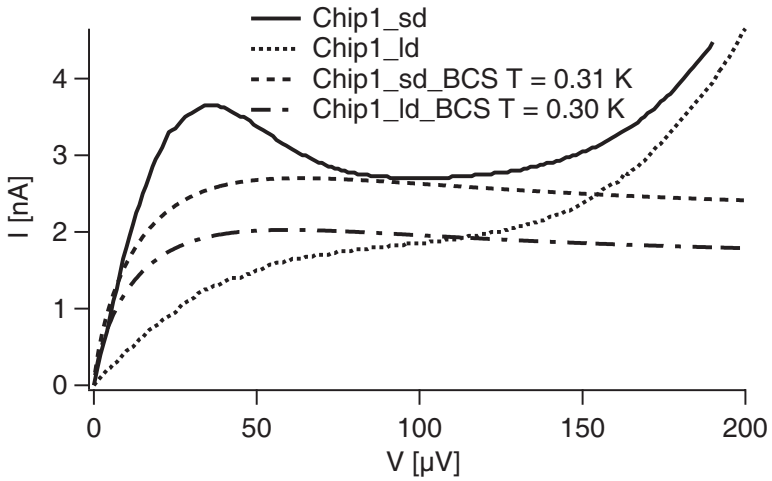

Figure 5.12: Current vs. voltage characteristic of the $\Delta = 170\,\mu eV$ devices.

We biased both devices around $110\,\mu V$ and recorded 4000 pulses for several light intensities (i.e. different average photon numbers). Figure 5.13 shows the histogram of the integrated pulse charge for 3 different intensities. The no-photon case, when the laser optical shutter is closed, tests how much of the energy distribution is due to the noise independent of the photon flux. The average pulse from Chip1_sd has a characteristic decay time of $10.7\,\mu s$ and a responsivity of 2330 electrons/eV. The long-diffusion engineered device, Chip1_ld, had a lower responsivity of 1840 electrons/eV, associated with a shorter pulse decay time of $9.6\,\mu s$.

The best energy resolution $\Delta E = 1.65$ eV was obtained with Chip1_ld. The energy distribution for both devices tested with the cold feedback resistor widened as the light intensity increases, as shown in Figure 5.14.

The charge offset represents the average integrated charge of the pulses recorded when no photons landed on the absorber. This variable is proportional to the light intensity, just like the energy distribution width. Figure 5.15 displays the measured charge offset for different light intensities, for both diffusion-engineered devices.

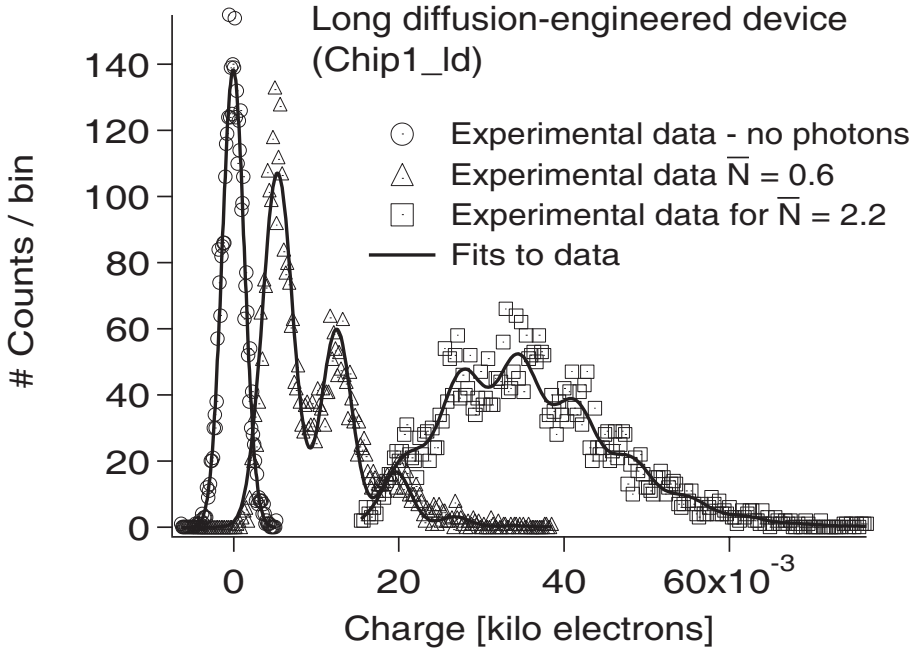

Figure 5.13: Pulse histograms for the clean Al, long diffusion-engineered device, tested at different light intensities, each corresponding to a different average photon number of the Poisson distribution.

5.3.4 Aluminum Devices with $\Delta = 225\ \mu eV$ (Chip2)

In order to obtain a smaller diffusion constant, we fabricated devices where the Al was deposited in the presence of oxygen. This Al is what we refer to as 'dirty' Al. The parameters for these devices are shown in Appendix B. The devices had a gap energy $\Delta = 225\ \mu eV$ and a normal state resistance $R_n = 90\ \Omega$. We tested three types of devices: single tunnel device (Chip2_st), 'short diffusion-engineered' device with a $0.25 \times 62\ \mu m^2$ outdiffusion lead (Chip2_sd), and 'long diffusion-engineered' device with a $0.25 \times 125\ \mu m^2$ outdiffusion lead (Chip2_ld).

The current vs. voltage characteristics of all three devices after the critical current has been optimally suppressed are shown in Figure 5.16. We notice the imperfect suppression of the critical current in all three devices.

The long diffusion-engineered device was tested in a slightly different setup, shown in Figure 5.17. We fabricated a mechanical mask by depositing 100 nm Au with a 3

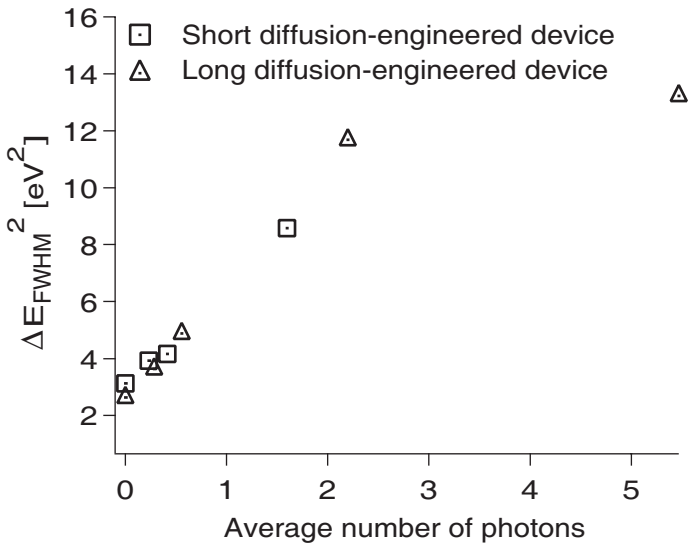

Figure 5.14: FWHM of the energy distribution for the $\Delta = 170\,\mu eV$ devices.

nm seed layer of Ti on a glass slide. The Au covered a $0.4 \times 1.6\,\mu m^2$ area, except for a central $61 \times 130\,\mu m^2$ rectangle which remained transparent. The glass slide was diced into a $0.6 \times 1.6\,mm^2$ rectangle. Two small pieces of the same glass slide were glued with GE-varnish on the top and bottom of the device chip, but far away from the detectors. The diced Au mask was placed on top of the two glued pieces, preventing the scratching of the device. It was then manually aligned such that the central transparent rectangle would sit on top of the detectors.

Laser pulses were recorded and analyzed for all three devices. Chip2_st had a responsivity of 1500 electrons/eV (5500 electrons/photon). The average pulse had a characteristic decay time $\tau = 4.3\,\mu s$. Chip2_sd showed a larger responsivity, 3500 electrons/eV, as well as a longer decay time $\tau = 9.1\,\mu s$. The device with the outdifussion lead twice as long as the one of Chip2_sd, Chip2_ld, had an intermediate value of its average pulse characteristic decay time, between that of the single-tunnel and that of the short-diffusion engineered devices, $\tau = 6.8\,\mu s$. Its responsivity was 2330 electrons/eV. Histograms from all three devices are shown in Figure 5.18, for the same number of average photons.

The offset charge Q_0 increased linearly with the tested flux of incoming photons. The

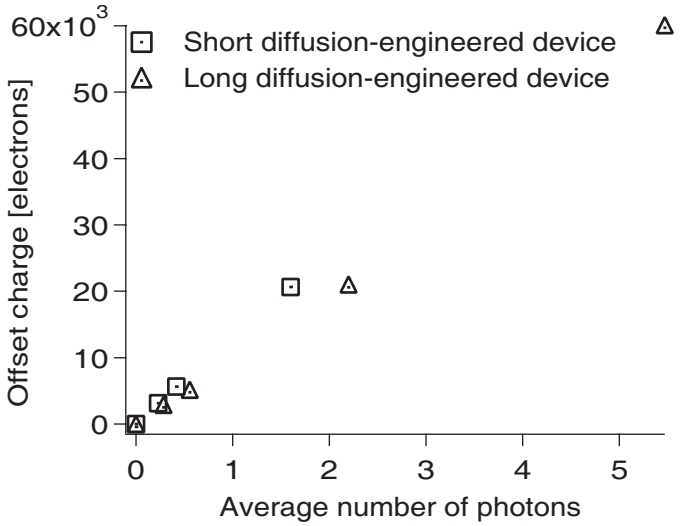

Figure 5.15: Charge offset vs. average number of photons for the $\Delta = 170\,\mu eV$ devices.

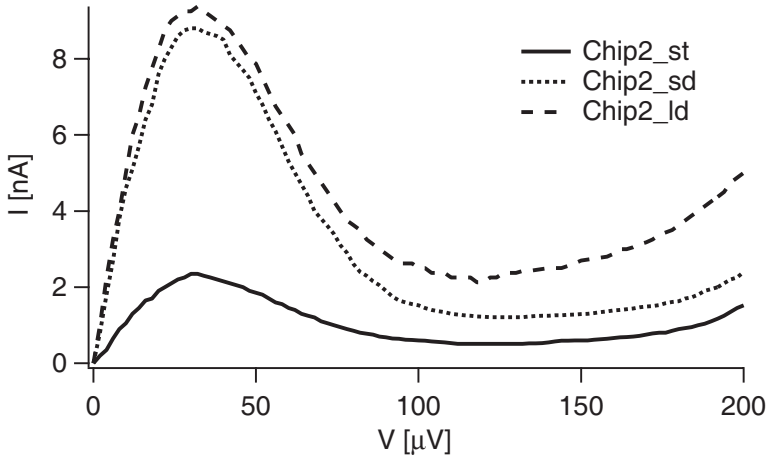

Figure 5.16: Current vs. voltage characteristic of the $\Delta = 225\,\mu eV$ devices.

three devices show different slopes, seen in figure 5.19.

The best energy resolution was obtained for Chip2_sd, $\Delta E = 1.23$ eV. Chip2_ld had $\Delta E = 1.72$ eV, followed by Chip2_st with $\Delta E = 1.8$ eV. The FWHM of the energy distribution increased with $\bar{N}$ for all devices.

Chip2_ld is the only device tested with photons from the Hg lamp. A violet filter allowed only photons of 2.85 eV of energy to be absorbed by the device. The signal trigger was set at a voltage equivalent to a 0.3 nA current. Most recorded pulses do not peak above 0.3 nA. This means that the average charge of the acquired pulses sets an

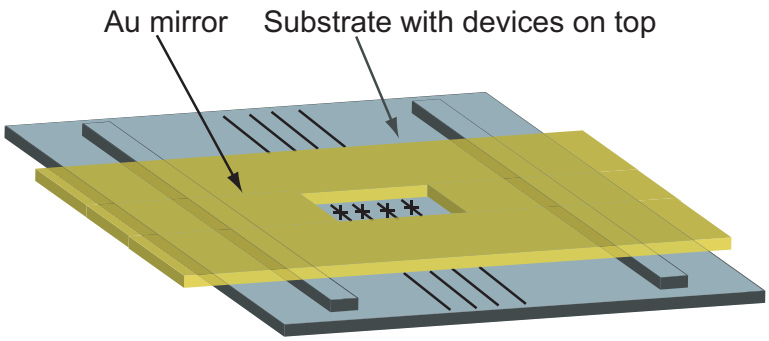

Figure 5.17: Microscope slide with Au deposited on it (Au mirror) everywhere except the center rectangle, sitting above the substrate on two rectangular pieces of glass and masking the area around the devices against impinging photons.

upper limit on the average charge created by the violet photons in our device. Figure 5.21 shows a typical pulse from the 2.85 eV photon on top of the average pulse from a 3.68 laser photon, taken during the same cooldown. The average number of photons in the laser experiment was $\bar{N} = 1.14$, the responsivity $R = 2440$ electrons/eV, and the charge offset $Q_0 = 7750$ electrons.

5.3.5 Aluminum Devices with $\Delta = 235\ \mu eV$ (Chip3)

We fabricated devices with an even higher concentration of oxygen in the Al electrodes. The parameters for these devices are shown in Appendix B. The devices had a gap energy Δ of 235 μeV and a normal state resistance of 50 Ω. We tested three types of devices: single tunnel device (Chip3_st), 'short diffusion-engineered' device with a $0.25 \times 15\ \mu m^2$ outdiffusion lead (Chip3_sd), and 'long diffusion-engineered' device with a $0.25 \times 62\ \mu m^2$ outdiffusion lead (Chip3_ld).

The current vs. voltage characteristic of these devices, with the best suppression of the critical current, is shown in Figure 5.22.

The decay times for all the tested devices in this category were less than 7 μs. The single tunnelling device had an average pulse decay time of 3.8 μs and a responsivity of 1750 electrons/eV. Chip3_sd had a longer average pulse decay time of 5.4 μs and a larger responsivity of 3000 electrons/eV. The long-diffusion engineered device has a pulse decay

time of 6 μs. The energy resolution of Chip3_ld was not good enough for single-photon detection.

Both the offset charge and the FWHM of the energy distribution increased with the average number of absorbed photons, as seen in Figure 5.23 and Figure 5.24.

5.3.6 Charge Multiplication

We analyze the signal increase in the diffusion-engineered devices by comparing the expected charge multiplication factor to its experimental value. From transport measurements we extract the resistance per square for our Al films. We measure structures identical to the diffusion-engineered wires in our devices. We then compute the normal state diffusion constant and and then infer the quasiparticle superconducting diffusion constant, which depends on the wire temperature [2]. We assume the junction temperature is the same as the outdiffusion wire temperature. The temperature is extracted from comparing the experimental value of the subgap current for a particular device to BCS simulations, at a bias voltage of $110\mu V$. In our experiments the diffusion constant for the superconducting state is reduced by a factor of $3-4$ compared to the normal state value.

Device	Δ $[\mu eV]$	D_n $[cm^2/s]$	T_{eff} [K]	D_{qp} $[cm^2/s]$	τ_{pulse} $[\mu s]$	τ_{out} $[\mu s]$
Chip1_st	170	26	0.29	8.0	4.9	–
Chip1_sd	170	26	0.31	8.2	10.7	10.5
Chip1_ld	170	26	0.30	8.1	9.6	15.4
Chip2_st	225	18	0.30	4.9	4.3	–
Chip2_sd	225	18	0.34	5.2	9.1	13.4
Chip2_ld	225	18	0.36	5.3	6.8	17.5
Chip3_st	235	6	0.34	1.7	3.8	–
Chip3_sd	235	6	0.34	1.7	5.4	10.8
Chip3_ld	235	6	0.39	1.8	6.0	18.3

Table 5.2: Diffusion constants, effective temperature, and predicted outdiffusion times for different devices.

[2]The structures were made in the same deposition process as the actual devices. They were fabricated a year later than the ones quoted in the 'Diffusion in Al' subsection, and had twice as large a diffusion constant.

We use the geometrical dimensions of our devices and the superconducting diffusion constant into the 2D diffusion simulation to extract the outdiffusion time τ_{out}. The outdiffusion time is computed as the time it takes 67% of the quasiparticles to leave the electrodes and wire area, including a certain loss (recombination) time. Table 5.2 shows the above parameters for our devices, including a loss time of 20 μs in the simulation for the outdiffusion time and the measured decay time of the pulses τ_{pulse}.

We see that a recombination time of 20 μs is compatible with the results from Chip1_sd device, while a shorter loss time would be consistent with the times obtained for Chip2 and Chip3 devices. Even within the same material type devices (such as devices on Chip1, Chip2, or Chip3) assuming the same loss time does not provide consistent results among the diffusion-engineered samples. This implies the possibility of a loss time related to the length of the outdiffusion lead. This could be the case if there were depressed-gap regions along the lead, which would facilitate quasiparticle trapping.

In Figure 5.25 we summarize our results. The simulated charge multiplication factor, p_{sim}, is computed as the ratio of the simulated outdiffusion time to the experimental tunnelling time. The ratio of the experimental pulse decay time for the diffusion-engineered devices to the tunnelling time is presented, along with the experimental charge gain factor (Q/Q_i). The two experimental ratios agree well with each other, as expected, but the number of times the quasiparticles tunnel does not exceed 2 in any of the devices. This discrepancy from the expected behavior is indicative of strong losses in our materials.

5.4 Summary

We succesfully tested single-tunnelling and diffusion-engineered devices with single UV photon resolution. The diffusion-engineered samples provided charge gain upon absorption of photons due to backtunnelling, compared to the single-tunnelling samples. The charge multiplication technique could not be tested to factors larger than 2.3 due to a relatively short loss time in our devices, on the order of 20 μs.

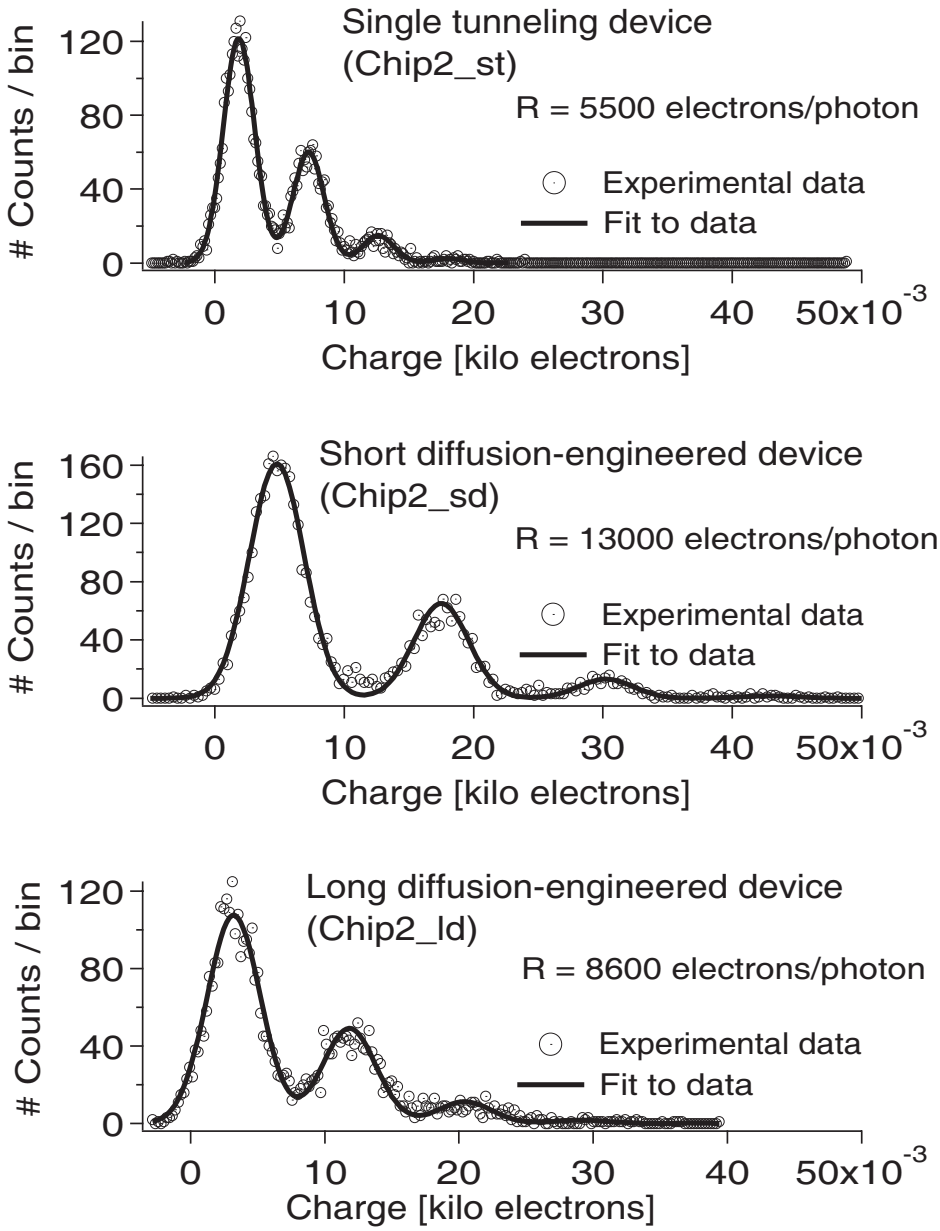

Figure 5.18: Pulse histograms from three different devices under laser testing. The average number of photons per pulse was around 0.5 for all.

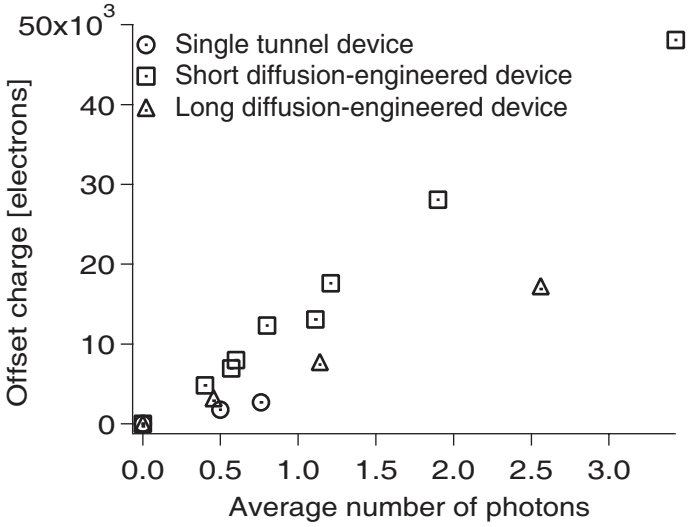

Figure 5.19: Charge offset Q_0 vs. average number of photons $\bar{N}$ for the $\Delta = 225\ \mu eV$ devices.

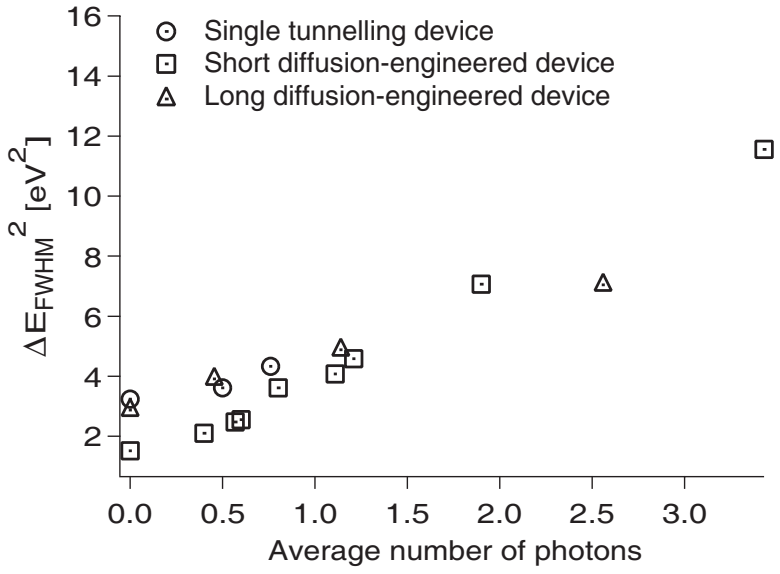

Figure 5.20: FWHM of the energy distribution for the $\Delta = 225\ \mu eV$ devices.

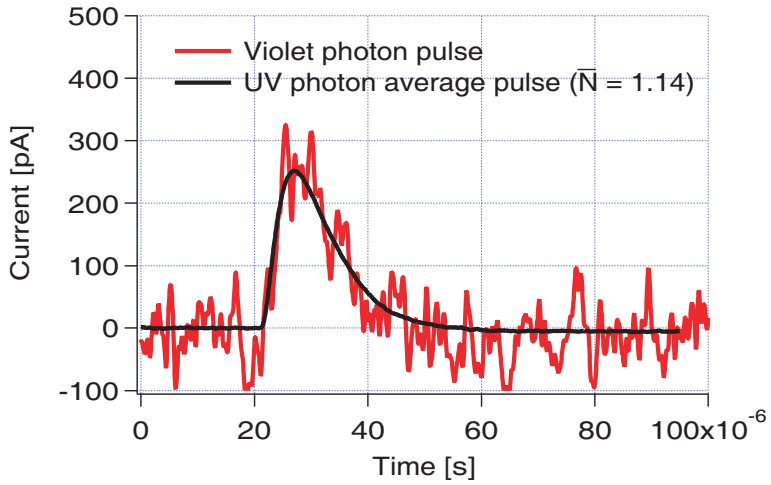

Figure 5.21: Violet photon single pulse and UV photons average pulse.

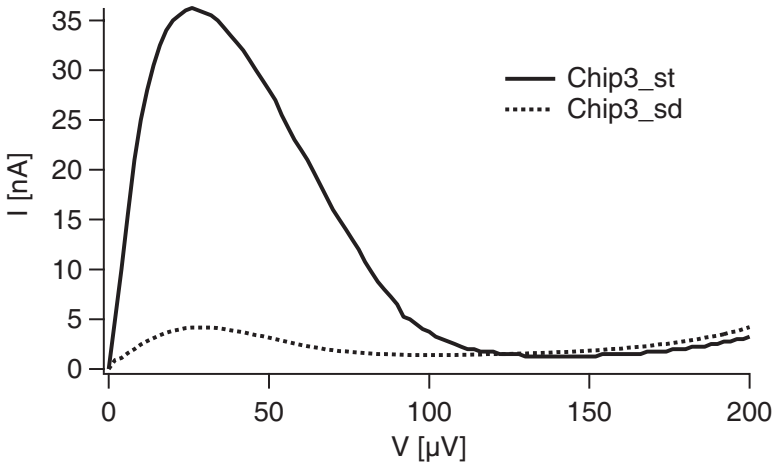

Figure 5.22: Current vs. voltage characteristic of the $\Delta = 235\,\mu eV$ devices.

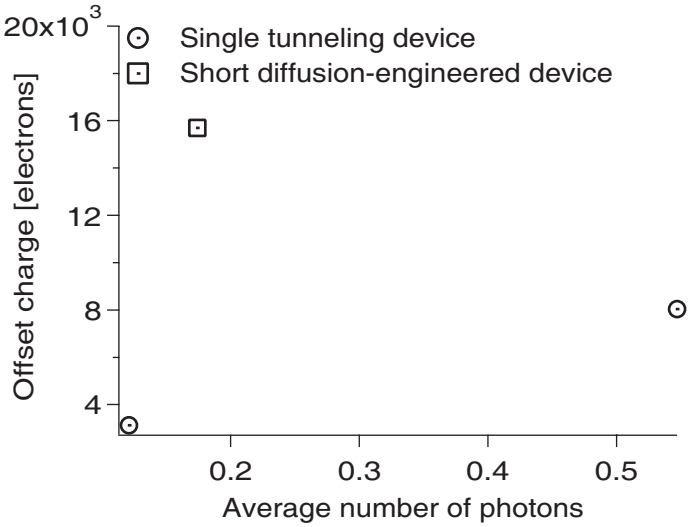

Figure 5.23: Charge offset vs. average number of photons for the $\Delta = 235\ \mu eV$ devices.

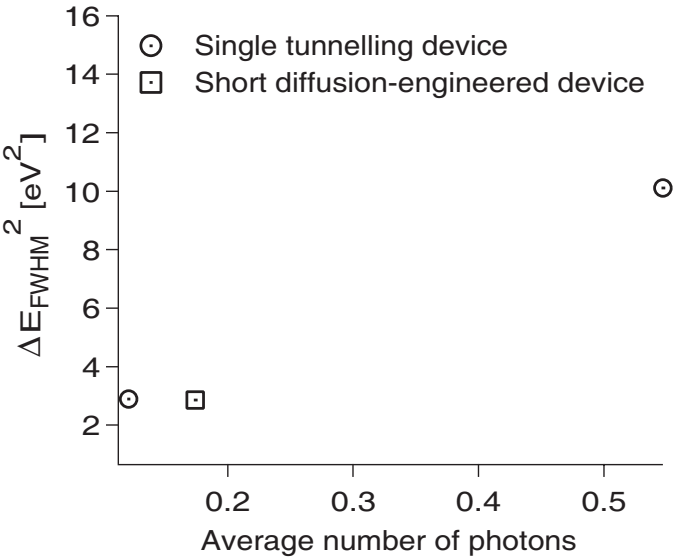

Figure 5.24: FWHM of the energy distribution for the $\Delta = 235\ \mu eV$ devices.

Device Type / Material	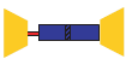		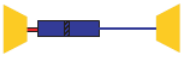
Chip1 D_{qp} = 8.1 cm²/s	Q_i = 4400 τ_{tunn} = 4.9 μs	Q/Q_i = 1.9 τ/τ_{tunn} = 2.2 p_{sim} = 3.6	Q/Q_i = 1.5 τ/τ_{tunn} = 1.9 p_{sim} = 7.3
Chip2 D_{qp} = 5.2 cm²/s	Q_i = 5500 τ_{tunn} = 4.3 μs	Q/Q_i = 2.3 τ/τ_{tunn} = 2.1 p_{sim} = 6.2	Q/Q_i = 1.5 τ/τ_{tunn} = 1.6 p_{sim} = 11.9
Chip3 D_{qp} = 1.7 cm²/s	Q_i = 6450 τ_{tunn} = 3.8 μs	Q/Q_i = 1.7 τ/τ_{tunn} = 1.4 p_{sim} = 4.5	Q/Q_i - τ/τ_{tunn} = 1.6 p_{sim} = 15.6

Figure 5.25: Results.

Chapter 6

Conclusions

6.1 Diffusion Engineering Review

We have developed an STJ-based spectrometer with single photon resolution in the UV spectrum. Previous work in our group used gap engineering to intrinsically amplify the signal created by an absorbed photon, using backtunnelling. The performance of those devices was limited by the generation-recombination noise [Wilson2001] of the quasiparticles confined in the Al electrodes by higher-gap Ta plugs.

We implemented a new approach, called diffusion engineering. In this approach the junction electrode terminates with a long and narrow lead that prevents quasiparticles from quickly diffusing away. The quasiparticles tunnel and backtunnel across the voltage-biased junction before they slowly diffuse out the lead or get lost through recombination or other loss mechanisms.

We designed, fabricated and tested single-tunnelling devices and devices with different outdiffusion lead lengths. We used $1 \times 5\ \mu m^2$ Al/AlOx/Al junctions, with $5 \times 10\ \mu m^2$ Al electrodes, which also functioned as the absorber. We fabricated Al films of different qualities, thus changing the diffusion constant in the outdiffusion lead, and therefore the outdiffsion time.

6.2 Device Performance

The diffusion-engineered devices have consistently shown an improved energy resolution over the single-tunnelling devices, as long as the loss time in the devices was longer than the outdiffusion time. The best energy resolving power $E/\Delta E = 3$ at 3.68 eV was obtained with the diffusion-engineered device Chip2_sd, where we successfully implemented back-tunnelling to obtain a charge multiplication factor of 2.3.

The devices showed single-photon resolution when tested with 3.68 eV photons from a pulsed UV laser, as well as at smaller energies (2.85 eV), when tested with single photons from a Hg lamp.

The diffusion-engineered devices should not be limited by the generation-recombination noise present in the gap-engineered devices. The SNR of our detectors will be increased by achieving a longer quasiparticle lifetime, thus having the possibility of increasing the signal, which is proportional to the charge multiplication factor. Further reduction of the noise sources present in our experiment will also increase the energy resolving power of our detectors, pushing their single-photon sensitivity to a lower photon energy.

6.3 Alternative Future Approaches

For future development of these devices, the nature of the loss mechanism in our detectors has to be investigated. A longer effective quasiparticle lifetime would allow the quasiparticles to tunnel and backtunnel for a longer time before they diffuse out. Thus, larger charge multiplication factors can be tested, increasing the SNR of our detectors.

Lowering the readout electronic noise is another step towards increasing the detectors' energy resolution. An alternative readout technique has been proposed [Prober2006NIMA] using a radio frequency (rf) reflection measurement, developed at Yale by Professor R. J. Schoelkopf for reading out the high-impedance Single Electron Transistor (SET). In this approach, the rf signal reflected from the STJ biased around zero voltage is monitored.

The reflected signal depends on the STJ impedance around zero bias, which provides a very sensitive measure of the number of excess quasiparticles. A resonant readout is used, opening the possibility of frequency multiplexing several STJs in an efficient fashion.

Testing devices at lower temperatures than those tested in this work would also be beneficial for achieving a higher energy resolving power, by decreasing the Johnson current noise of the STJ. Once the detector resolution is limited by statistical noise, lower-gap materials should be used as the absorber. This would increase the SNR as the square root of Δ^{-1}, although the relaxation time for quasiparticles becomes longer, which is detrimental to the photon counting rate and increases the importance of any loss in the materials.

Appendix A

Film Properties

The Ta thicknesses on wafers E04 and AP05 are 85 nm and 70 nm respectively. The aluminum films on Al1 and Al2 was deposited in the Plassys in the presence of 0.4 sccm of oxygen. Both films had a first 50 nm layer deposited (thickness perpendicular to the substrate) at a 40° angle from the normal; this was oxidized at the parameters listed below; then a second 70 nm layer was deposited normal to the surface. The oxidation parameters for the two films are: 20 Torr for 12 min for Al1; 3 Torr for 10 minutes for Al2. The resistance for the Al films was measured for both films, with the total thickness of 120 nm, and the oxide layer in between.

Film type	Dimensions [μm^2]	Resistance @ 300 K [Ω]	RRR	R/square [Ω]
	1×20	61.6	7.3	3
Ta [wafer E04]	1×30	82.4	7.0	3
$T_C = 4.4$ K	2×20	38.4	7.1	3
d = 85 nm	2×40	59	7	3
	0.15×4.5	103	4.12	3
Ta [wafer E04]	0.3×6	62.5	6.25	3
$T_C = 4.4$ K	0.3×9	115	4.6	3
d = 85 nm	0.3×12	136	5.4	3
	2.3×140	309.2	4.12	1.64
Ta [wafer AP05]	2.4×100	231.2	6.25	1.87
$T_C = 4.05$ K	2.3×140	323.5	4.6	1.73
d = 70 nm	2.3×170	390.6	5.4	1.71
Al 1	2.2×160	62.3	0.86	1
20 Torr×12 min	2.2×120	52.9	0.95	1
Al 2	0.25×60	248	1.3	0.85
3 Torr×10 min	0.25×120	529	1.3	0.85

Table A.1: Properties of Ta and Al films.

Appendix B

Device Parameters

Sample	Al type	Energy gap [μeV]	Normal Resistance [Ω]
Chip1_ st (AP05_Diff1_3_1st)	clean (Lesker)	170	133
Chip1_ sd (AP05_Diff1_3_1st)	clean (Lesker)	170	133
Chip1_ ld (AP05_Diff1_3_1st)	clean (Lesker)	170	133
Chip2_ st (AP05_Diff1_3_2nd)	dirty (Plassys)	225	90
Chip2_ sd (AP05_Diff1_3_2nd)	dirty (Plassys)	225	90
Chip2_ ld (AP05_Diff1_3_2nd)	dirty (Plassys)	225	90
Chip3_ st (AP05_Diff1_7_1st)	dirtier (Plassys)	235	50
Chip3_ sd (AP05_Diff1_7_1st)	dirtier (Plassys)	235	50
Chip3_ ld (AP05_Diff1_7_1st)	dirtier (Plassys)	235	50

Table B.1: Device Parameters - the normal resistance was measured at voltages $> 2\Delta$ and at a temperature $T << T_C$.

Sample	Outdiffusion wire [μm^2]	Run date	Responsivity [e^-/eV]	Offset charge [e^-]	Average photon number	Energy FWHM [eV]	Pulse fall time [μs]
Chip1_ st	0	11/09/05	1200	16300	3	4.2	4.9
Chip1_ sd	0.25×62	01/16/06	2300	5600	0.4	2	10.7
Chip1_ ld	0.25×125	01/16/06	1900	5200	0.56	2.23	9.6
Chip2_ st	0	01/30/06	1460	1800	0.5	1.9	4.3
Chip2_ sd	0.25×62	01/30/06	3500	4800	0.4	1.45	9.1
Chip2_ ld	0.25×125	03/20/06	2350	3220	0.46	2	6.8
Chip3_ st	0	02/21/06	1750	8050	0.55	3.18	3.8
Chip3_ st	0	02/21/06	1950	3120	0.12	1.7	5.4
Chip3_ sd	0.25×15	02/21/06	3000	15700	0.17	1.69	6.0

Table B.2: Important Runs and Selected Results

Bibliography

[Anthore2003] A. Anthore, H. Pothier, and D. Esteve. Density of states in a superconductor carrying a supercurrent. *Physical Review Letters*, 90(12):127001, 2003.

[BCS1957] J. Bardeen, L. N. Cooper, and J. R. Schrieffer. Theory of superconductivity. *Physical Review*, 108(5).

[Booth1987] N. E. Booth. Quasiparticle trapping and the quasiparticle multiplier. *Applied Physics Letters*, 50:293, 1987.

[Bruijne2002] J. H. J. de Bruijne, A. P. Reynolds, M. A. C. Perryman, A. Peacock, F. favata, N. Rando, D. Martin, P. Verhoeve, and N. Christlieb. Direct determination of quasar redshifts. *Astronomy and Astrophysics*, 381, 2002.

[Dolan1977] G. J. Dolan. Offset masks for lift-off photoprocessing. *Applied Physics Letters*, 31(5):337, 1977.

[Ehrenreich1963] H. Ehrenreich, H. R. Philipp, and B. Segall. Optical properties of aluminum. *Physical Review*, 132(5):1918, 1963.

[Friedrich1997] Stephan Friedrich. *Superconducting single photon imaging X-ray spectrometers*. PhD thesis, Yale University, 1997.

[Friedrich97IEEE] S. Friedrich, K. Segall, M. C. Gaidis, C. M. Wilson, D. E. Prober, P. J. Kindlemann, A. E. Szymkowiak, and S. H. Moseley. Single pho-

ton imaging X-ray spectrometers using low noise current preamplifiers with dc voltage bias. *IEEE Transactions on Applied Superconductivity*, 7(2):3383, 1997.

[Gaidis1994] Michael Gaidis. *Superconducting tunnel junctions as single photon X-ray detectors*. PhD thesis, Yale University, 1994.

[Goldie1994] D. J. Goldie, P. L. Brink, C. Patel, N. E. Booth, and G. L. Salmon. Statistical noise due to tunneling in superconducting tunnel junctions. *Applied Physics Letters*, 64:3169, 1994.

[Golubov1994] A. A. Golubov, E. P. Houwman, J. G. Gijsbertsen, J. Flokstra, and H. Rogalla. Quasiparticle lifetimes and tunneling times in a superconductor-insulator-superconductor tunnel junction with spatially inhomogeneous electrodes. *Phsical Review B*, 49(18):12953, 1994.

[Gray1978] K. E. Gray. A superconducting transistor. *Applied Physics Letters*, 32:392, 1978.

[Kaplan1976] S. B. Kaplan, C. C. Chi, and D. N. Langenberg. Quasiparticle and phonon lifetimes in superconductors. *Physical Review B*, 14(11):4854, 1976.

[Kittel] C. Kittel. *Introduction to Solid State Physics*. John Wiley and Sons, Inc.

[Kozorezov2000] A. G. Kozorezov, A. F. Volkov, J. K. Wigmore, A. Peacock, A. Poelaert, and R. den Hartog. Quasiparticle-phonon downconversion in nonequilibrium superconductors. *Physical Review B*, 61(17):807, 2000.

[Kurakado1982] M. Kurakado. Possibility of high resolution detectors using superconducting tunnel junctions. *Nuclear Instruments and Methods*, 196:275, 1982.

[LSM510] Carl Zeiss, Inc. Meta laser scanning microscope 510 data sheet.

[Li2002] Liqun Li. *X-ray Single Photon Imaging Detectors using Superconducting Tunnel Junctions*. PhD thesis, Yale University, 2002.

[McMillan1966] W. L. McMillan and P. W. Anderson. Theory of geometrical resonances in the tunneling charcateristics of thick films in superconductors. *Physical Review Letters*, 16(3):85, 1966.

[Nagl2005] S. Nagl, M. Schaeferling, and O. S. Wolfbeis. Fluorescence analisys in microarray technology. *Microchimica Acta*, 151:1, 2005.

[Narayanamurti1978] V. Narayanamurti, R. C. Dynes, P. Hu, H. Smith, and W. F. Brinkman. Quasiparticle and phonon propagation in bulk, superconducting lead. *Physical Review B*, 18(11).

[Prober2006] Invited Talk by Daniel Prober at the Applied Superconductivity Conference in Seattle. Ultra-sensitive quantum-limited far-infrared stj detectors, http://www.yale.edu/proberlab/stj.html. 2006.

[Prober2006NIMA] D. E. Prober, J. D. Teufel, L. Frunzio, C. M. Wilson, and R. J. Schoelkopf. Quasiparticle dynamics and a new, high-resolution readout of stj photon detectors. *Nuclear Intruments and Methods in Physics Research A*, 559:676, 2006.

[Rando1992] N. Rando, A. Peacock, A. van Dordrecht, C. Foden, R. Engelhardt, B. G. Taylor, P. Gare, J. Lumley, and C. Pereira. The properties of niobium superconducting tunneling junctions as X-ray detectors. *Nuclear*

Instruments and Methods in Physics Research Section A: Accelerators, Spectrometers, Detectors and Associated Instruments, 313:173, 1992.

[Rando2000] N. Rando, S. Andersson, B. Collaudin, F. Favata, P. Gondoin, A. Peacock, M. Perryman, J. Verveer, P. Verhoeve, and D. J. Goldie. First astronomical results from S-Cam. *Nuclear Instruments and Methods in Physics Research Section A: Accelerators, Spectrometers, Detectors and Associated Instruments*, 444(1):441, 2000.

[Rothwarf1967] A. Rothwarf and B. N. Taylor. Measurement of recombination lifetimes in superconductors. *Physical Review Letters*, 19(1):27, 1967.

[Segall2000] Kenneth Segall. *Noise and Quasiparticle Dynamics in Single Photon, Superconducting Tunnel Junctions Detectors*. PhD thesis, Yale University, 2000.

[Segall2004] K. Segall, C. Wilson, L. Li, S. Friedrich, M. C. Gaidis, and D. E. Prober. Dynamics and energy distribution of nonequilibrium quasiparticles in superconducting tunnel junctions. *Physical Review B*, 70:214520, 2004.

[Subgap2001] M. A. Gubrud, M. Ejrnaes, A. J. Berkley, R. C. Ramos Jr., I. Jin, J. R. Anderson, A. J. Dragt, C. J. Lobb, and F. C. Wellstood. Sub-gap leakage in nb/alo$_x$/nb and al/alo$_x$/al josephson junctions. *IEEE Transaction on Applied superconductivity*, 11(1):1002, 2001.

[Teufel2007] John Teufel. *Superconducting Tunnel Junctions as Direct Detectors for Submillimeter Astronomy*. PhD thesis, Yale University, 2007.

[Tinkham1972] Michael Tinkham. Tunneling generation, relaxation, and tunneling detection of hole-electron imbalance in superconductors. *Physical Review B*, 6:1747, 1972.

[Tomasch1966] W. J. Tomasch. Geometrical resonance and boundary effects in tunneling from superconducting In. *Physical Review Letters*, 16(1):16, 1966.

[Twerenbold1986] D. Twerenbold. Nonequilibrium model of the superconducting tunneling junction X-ray detector. *Physical Review B*, 34(11):7748, 1986.

[VanDuzer1981] T. Van Duzer and C. W. Turner. *Principles of superconductive devices and circuits*. Elsevier, 1981.

[Verhoeve2006] P. Verhoeve, D. Martin, R. A. Hijmering, J. Verveer, A. van Dordrecht, G. Sirbi, T. Oosterbroek, and A. Peacock. S-Cam 3: Optical astronomy with a STJ-based imaging spectrophotometer. *Nuclear Instruments and Methods in Physics Research A*, 559:598, 2006.

[Weaver1974] J. H. Weaver, D. W. Lynch, and C. G. Olson. Optical properties of V, Ta, and Mo from 0.1 to 35 eV. *Physical Review B*, 10(2):501, 1974.

[Wilson2001] C. M. Wilson, L. Frunzio, and D. E. Prober. Time-resolved measurements of thermodynamic fluctuations of the particle number in a nondegenerate fermi gas. *Physical Review Letters*, 87(6):067004, 2001.

[Wilson2002] Christopher M. Wilson. *Optical/UV single-photon spectrometers using superconducting tunnel junctions*. PhD thesis, Yale University, 2002.